

# SOFC anode modelling using TPB based kinetics

JINJUN LI

Master of Science Thesis



# **SOFC anode modelling using TPB based kinetics**

A thesis submitted for the degree of Master of Science in  
Sustainable Energy Technology at Delft University of Technology

**JINJUN LI**

September 2017

Sustainable Energy Technology, EEMCS faculty,  
Delft University of Technology

## **Graduate**

JINJUN LI

MSc Sustainable Energy Technology

Faculty of Electrical Engineering, Mathematics and Computer Science (EEMCS)

## **Supervisors**

Assoc.Prof P.V.Aravind

Dr. AN Tabish

## **MSc Thesis Committee**

Associate Professor P.V. Aravind

Professor D.J.E.M. Roekaerts

Assistant Professor W.F. Jager

## **Delft University of Technology**

Department of Process and Energy

# Abstract

Fuel cells directly convert chemical energy to electrical energy. Thanks to their highly efficient operation and eco-friendly performance, fuel cells have become promising energy converters to power the future. Solid oxide fuel cell as one kind of fuel cells, exhibits its advantages such as fuel variability. Capable of running on renewable fuels like biomass, SOFCs are regarded as potential solution to carbon-neutral energy conversion path. SOFCs operate on fuel supplied to the anode and oxidant supplied to the cathode. The anode is ought to facilitate the oxidation of fuel and transport of electrons from the reaction site to the current collector. It should also enable the diffusion of gaseous fuel to the reaction sites and reaction products away from the reaction sites. Meeting abovementioned requirements, Ni/YSZ cermets are competent SOFC anodes, where Ni is an electronic conductor, YSZ is an ionic conductor, and pores in between Ni and YSZ facilitate the fuel supply. Fuel oxidation is believed to occur in the vicinity of triple phase boundaries (TPBs), where Ni particles, YSZ particles and pore interact. Thus, TPB length quantifies the electrochemically active sites within the anode. The fuel oxidation involves physical processes and multi-elementary reaction steps in reality, among which exists a rate-limiting step. The overall reaction rate can be represented by the rate-limiting step whose kinetics are proposed as a function of the TPB length. In many past computational studies of the cermet anode, a global electrochemical reaction expressed by Butler-Volmer equation is put forward, simplifying electrode reaction to a single step process and probably inadequately to present insights into intrinsic processes occurring within the anode. In this work, TPB-based kinetics, derived from the pattern anode experiment, are implemented in a CFD model to evaluate the performance of Ni/YSZ cermet-based cells. For model validation, simulated polarization curves are compared with the experimental ones. TPB length as a fitting parameter is determined to ensure the agreement between simulated polarization curves and experimental ones. The fitted TPB length is found to be several orders of magnitudes lower than physical TPB length of typical Ni-YSZ cermet anode, which might imply that only a small fraction of the physical TPB length actually participates in the electrochemical reactions. CFD behavior like species distribution and electrochemical behavior like overpotential breakdown are investigated. The gradient of species molar fraction in anode turns to be larger than that in fuel channel, agreeing with the fact that fluid flow is much slower in anode where species transport in porous electrode is dominated by diffusion rather than convection. The cathode activation overpotential makes the most significant contribution to the overall overpotential. The anode activation overpotential at high current density region in the case of low molar fraction of inlet hydrogen yields rapid increase, which could be explained as a consequence of rapid decrease of exchange

current density in the vicinity of anode/electrolyte interface. Parametric study of operating temperature is conducted later to see its effect on the cell performance. The higher the operating temperature is, the slower drop of cell voltage with respect to cell current is observed. At a fixed cell voltage, an elevated temperature will cause intensified fuel consumption/vapor generation within anode, leading to a larger gradient of species molar fraction and accordingly a larger concentration overpotential.

Keywords: SOFC, Ni/YSZ anode, TPB length, rate-limiting step, TPB-based kinetics

# Contents

<b>Abstract</b> .....	<b>i</b>
<b>Nomenclature</b> .....	<b>v</b>
<b>Introduction</b> .....	<b>1</b>
1.1 Fuel cell origin.....	1
1.2 Fuel cell types .....	1
1.3 SOFC operation .....	3
1.4 SOFC advantages and applications .....	3
1.5 SOFC configurations .....	4
1.6 SOFC anode.....	5
1.7 TPB-based kinetics in SOFC anode.....	6
1.8 Thesis objective .....	7
1.9 Thesis outline .....	7
<b>Literature Survey</b> .....	<b>8</b>
2.1 Polarization behavior .....	8
2.1.1 Activation overpotential .....	8
2.1.2 Ohmic overpotential.....	9
2.1.3 Concentration overpotential .....	9
2.2 Hydrogen oxidation at Ni/YSZ anode.....	10
2.2.1 Charge-transfer mechanisms .....	10
2.2.2 Rate-limiting step .....	12
2.3 Oxygen reduction at cathode .....	14
2.4 TPB length in anode.....	14
<b>Model Development</b> .....	<b>16</b>
3.1 Purposes and assumptions.....	16
3.2 Geometry and materials.....	16
3.3 Multiphysics modelling.....	17
3.3.1 Electrochemistry .....	18
3.3.2 Computational fluid dynamics -- Species transport.....	22
3.3.3 Computational fluid dynamics – Gas flow distribution .....	25
3.4 Methodology and Software .....	28
3.4.1 Discretization .....	28
3.4.2 Mesh.....	28
3.4.3 Convergence.....	30

<b>Results and Discussion .....</b>	<b>33</b>
4.1 Polarization curve .....	34
4.2 Distribution of gas species .....	36
4.3 Overpotential breakdown.....	38
4.4 Effect of temperature .....	45
<b>Conclusions and Outlook .....</b>	<b>51</b>
5.1 Conclusions .....	51
5.2 Outlook.....	51
<b>Acknowledgements .....</b>	<b>53</b>
<b>Bibliography .....</b>	<b>54</b>

## Nomenclature

$a_i$	chemical activity of species $i$	
$b_i$	Langmuir parameter of species $i$	$1/Pa$
$c_{i,TPB}$	concentration of species $i$ at TPB	$mol/m^3$
$c_i$	local intrinsic concentration of species $i$ at site adjacent to TPB	$mol/m^3$
$c_{i,b}$	concentration of species $i$ in bulk phase	$mol/m^3$
$D_{ik}$	binary diffusivity of species $i$ and species $k$	$m^2/s$
$D_{iM}$	Knudsen diffusivity of species $i$	$m^2/s$
$D_i$	diffusivity of species $i$	$m^2/s$
$D_{i,s}$	surface diffusivity of species $i$	$m^2/s$
$E_{rev}$	cell reversible potential	$V$
$E_a$	anode potential	$V$
$E_c$	cathode potential	$V$
$E_{e,a}$	electrolyte potential at electrolyte/anode interface	$V$
$E_{e,c}$	electrolyte potential at electrolyte/cathode interface	$V$
$\Delta E_{a/e}$	electric-potential difference between the anode and electrolyte	$V$
$\Delta E_{c/e}$	electric-potential difference between the cathode and electrolyte	$V$
$F$	Faraday constant (96500)	$c/mol$
$g$	molar Gibbs free energy	$J/mol$
$h$	molar enthalpy	$J/mol$
$I$	identity matrix	
$i$	current density	Consistent unit
$i_l$	TPB length-specific current	$A/m$
$i_a$	area-specific current	$A/m^2$
$i_v$	volume-specific current	$A/m^3$
$i^0$	exchange current density	Consistent unit
$k_f$	forward reaction rate constant	Consistent unit
$k_r$	reverse reaction rate constant	Consistent unit
$K$	equilibrium constant	
$l_{a,TPB}$	area-specific TPB length	$m/m^2$
$l_{v,TPB}$	volume-specific TPB length/TPB density	$m/m^3$
$M_i$	molar weight of species $i$	$g/mol$
$\dot{m}_{an}$	inlet mass flow rate of fuel	$kg/s$
$\dot{m}_{ca}$	inlet mass flow rate of air	$kg/s$

$n$	number of electrons	
$p_0$	standard pressure (1)	<i>atm</i>
$p_i$	partial pressure of species $i$	<i>Pa</i>
$Q$	volumetric charge source	$A/m^3$
$\dot{Q}_{an}$	volumetric flow rate at fuel channel inlet	$m^3/s$
$\dot{Q}_{ca}$	volumetric flow rate at fuel channel inlet	$m^3/s$
$R$	universal gas constant (8.314)	$\frac{J}{mol \cdot K}$
$r_p$	electrode pore radius	$m$
$R_{Ohm}$	area-specific resistance	$\Omega \cdot m^2$
$R_i$	chemical mass source term of species $i$	$\frac{kg}{m^3 \cdot s}$
$s$	molar entropy	$\frac{J}{mol \cdot K}$
$t$	time	$s$
$T$	temperature	$K$
$u$	velocity	$m/s$
$V_i$	diffusion volume of species $i$	
$x_i$	molar fraction of species $i$	
$\alpha_a$	anodic charge transfer coefficient	
$\alpha_c$	cathodic charge transfer coefficient	
$\beta_a$	anodic symmetric factor	
$\beta_c$	cathodic symmetric factor	
$\sigma$	conductivity	$S/m$
$\varepsilon$	electrode porosity	
$\tau$	electrode tortuosity	
$\kappa$	electrode permeability	$m^2$
$\rho_i$	density of species $i$	$kg/m^3$
$\mu_i$	fluid dynamic viscosity	$Pa \cdot s$
$\nu_i$	stoichiometric coefficient of species $i$	
$\eta_{act}$	activation overpotential	$V$
$\eta_{Ohm}$	Ohmic overpotential	$V$
$\eta_{con}$	concentration overpotential	$V$
OCV	open circuit voltage	$V$

# 1

## Introduction

### 1.1 Fuel cell origin

The world is now being haunted by several environmental challenges like global warming, air pollution and acid precipitation. On the other hand, increasing global population calls for an escalating energy supply. Considering fossil fuels are being depleted day after day, development of innovative power generation technologies is highly wanted. As an efficient and effective solution to environmental problems and energy need, fuel cell comes into people's view [1].

Fuel cells are energy converters, directly transforming chemical energy to electrical energy through electrochemical combination of gaseous fuel and oxidant gas [1]. Attempts to develop fuel cells as power sources have been made over many years. At the very beginning, they were created for space and defense applications, thanks to their compactness and high-energy renewability [2].

Compared to conventional power devices, fuel cells have their unique advantages:

1. Unlike diesel or gas engines, fuel cell efficiency is not limited by the Carnot cycle. A general fuel cell efficiency is reported to fall in the range between 40% and 60% [3].
2. Different from internal combustion engines, fuel cells are favored for their silent operation, making it a suitable power source within buildings such as hospitals.
3. In contrast to batteries, fuel cells rely on continuous supply of fuel and oxidant other than energy stored in chemicals. During operation, fuel cells serve as sustaining power source as long as fuel and oxidant are supplied.
4. Emitting orders of magnitude lower pollutant output than traditional technologies, fuel cells can mitigate pollution resulting from burning fossil fuels. For instance, the final products of Polymer Electrolyte Membrane Fuel Cell (PEMFC) is moisture only.

### 1.2 Fuel cell types

Judging from chemical characteristics of electrolyte as ion conductor, fuel cells could be categorized into different groups [3][4].

1. Polymer Electrolyte Membrane Fuel Cell (PEMFC)

- Common Electrolyte: perfluoro sulfonic acid
- Operating Temperature: 50 – 100°C
- Typical System Size: 1kW – 250kW
- Efficiency: 60% (transportation) & 35% (stationary)
- Applications: backup power, portable power, distributed generation, transportation, and specialty vehicles
- Advantages: solid electrolyte reducing corrosion and electrolyte management problems, low temperature, and quick start-up
- Disadvantages: expensive catalysts, sensitive to fuel impurities, low temperature waste heat

## 2. Alkaline Fuel Cell (AFC)

- Common Electrolyte: Aqueous solution of potassium hydroxide soaked in a matrix
- Operating Temperature: 90 – 100°C
- Typical System Size: 10kW – 100kW
- Efficiency: 60%
- Applications: Military and space
- Advantages: Low cost components; high performance resulting from faster cathode reaction
- Disadvantages: Sensitive to  $CO_2$  in fuel and air and difficult in electrolyte management

## 3. Phosphoric Acid Fuel Cell (PAFC)

- Common Electrolyte: Phosphoric acid soaked in a matrix
- Operating Temperature: 150 – 200°C
- Typical System Size: 50kW – 1MW
- Efficiency: 40%
- Applications: Distributed generation
- Advantages: CHP configuration enabled by high temperature; increased tolerance to fuel impurities
- Disadvantages: High cost of Pt catalyst; long start-up time; low current and power

## 4. Molten Carbonate Fuel Cell (MCFC)

- Common Electrolyte: Solution of lithium, sodium, and /or potassium carbonates, soaked in a matrix
- Operating Temperature: 600 – 700°C
- Typical System Size: 1kW – 1MW
- Efficiency: 45% – 50%
- Applications: Electric utility and distributed generation
- Advantages: High efficiency; fuel flexibility; diversity of catalysts; suitability for CHP
- Disadvantages: High temperature corrosion and breakdown of cell components; long start-up time; low power density

## 5. Solid Oxide Fuel Cell (SOFC)

- Common Electrolyte: Ytria stabilized zirconia
- Operating Temperature: 700 – 1000°C
- Typical System Size: 1kW – 3MW
- Efficiency: 60%
- Applications: Auxiliary power; electric utility; distributed generation
- Advantages: High efficiency; fuel flexibility; diversity of catalysts; solid electrolyte; suitability for CHP of hybrid GT-integrated cycle
- Disadvantages: High temperature corrosion and breakdown of cell components; long start-up time

The first 3 types are characterized by their low to medium temperature of operation (50 – 200°C). The latter 2 types are characterized by their high temperature of operation (600 – 1000°C), their ability to operate on diverse fuels such as methanol and their possibly high efficiency with heat recovery.

### 1.3 SOFC operation

Among the abovementioned fuel cell types, the SOFC is characterized by its ceramic electrolyte. As illustrated in Figure 1.3, a representative SOFC encompasses two electrodes.  $H_2$  as the fuel, is supplied to the anode side, where it is oxidized to produce  $H_2O$ , releasing free electrons;  $O_2$  as the oxidant, is supplied to the cathode side, where it is reduced to  $O^{2-}$ , accepting free electrons coming from the anode side. An external electric circuit bridges anode and cathode, allowing free electrons to pass from the anode to the cathode; The electrolyte connects cathode and anode, permitting  $O^{2-}$  to migrate from the cathode to the anode.

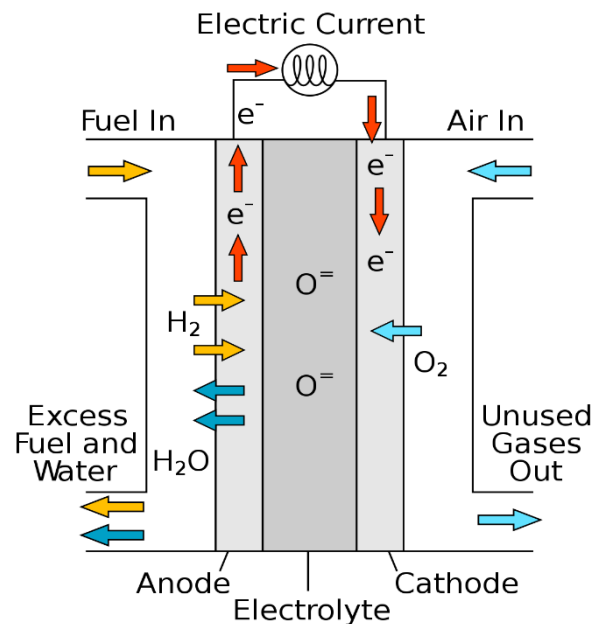


Figure 1.1 Schematic of SOFC operation [5]

### 1.4 SOFC advantages and applications

On top of general advantages of fuel cells summarized before, SOFC has its special competitiveness.

1. SOFCs have the highest overall fuel to electric efficiency among fuel cells currently being developed globally. For currently available commercial SOFCs, an efficiency of 60% can be reached [6]. Moreover, due to high exhaust gas temperature, a possibility of CHP implementation can be expected. For such hybrid systems, an overall efficiency of 85% can be achieved [6]. In addition, the high temperature exhaust gas can be supplied to a gas turbine to realize an SOFC-GT hybrid system where the system efficiency of 80% can be achieved [7].
2. SOFCs are adaptable in terms of fuel types. Not only hydrogen but also carbon-based fuels like natural gas can be supplied. In addition, solid oxide fuel cell can be fueled by renewable energy source such as biomass, realizing a carbon-neutral energy conversion path [6].
3. SOFCs do not require noble metals such as Pt which can be problematic in resource availability and price issue in high volume manufacture [1].
4. SOFCs are free from liquid electrolyte which can be corrosive and cause handling problems [1].

Based on the abovementioned advantages, SOFCs have extensive range of applications. Thanks to their high conversion efficiencies, SOFCs are suitable for distributed generation like stationary power where fuel costs a lot due to long delivery chain to end customers.

## 1.5 SOFC configurations

There are two common configurations of SOFCs. One configuration exhibits tubular geometry where tube consists of an assembly of electrodes and electrolyte in between, with fuel flowing by the external surface of tube and oxidant flowing by the internal surface of tube, as can be seen in Figure 2.1.

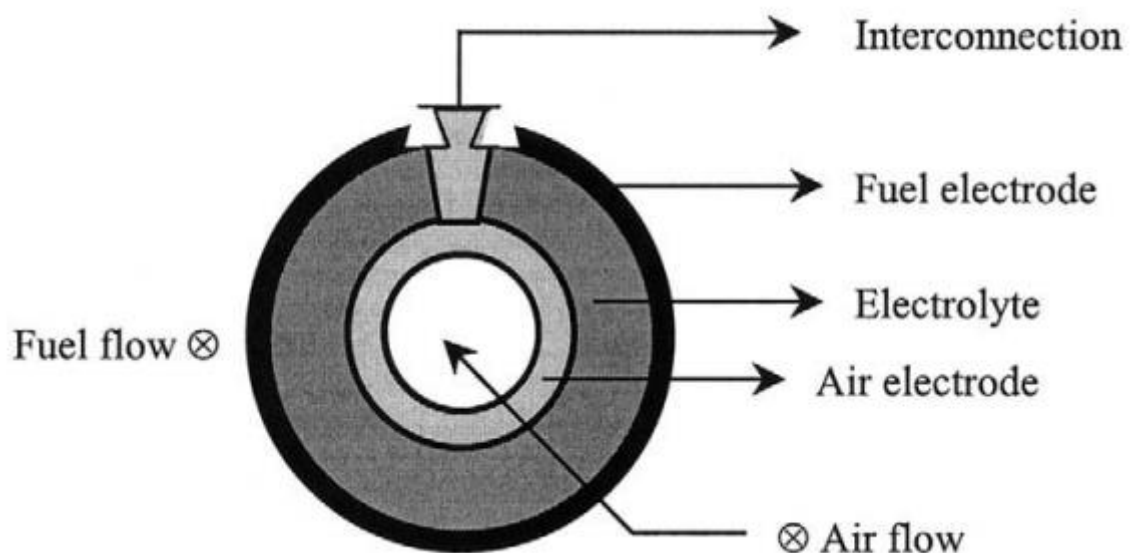


Figure 2.1 Typical tubular SOFC configuration [1]

Another configuration demonstrates planar geometry where electrolyte is sandwiched between electrodes,

with fuel and oxidant flowing through channels on one side of electrode face, as can be seen in Figure 1.3.

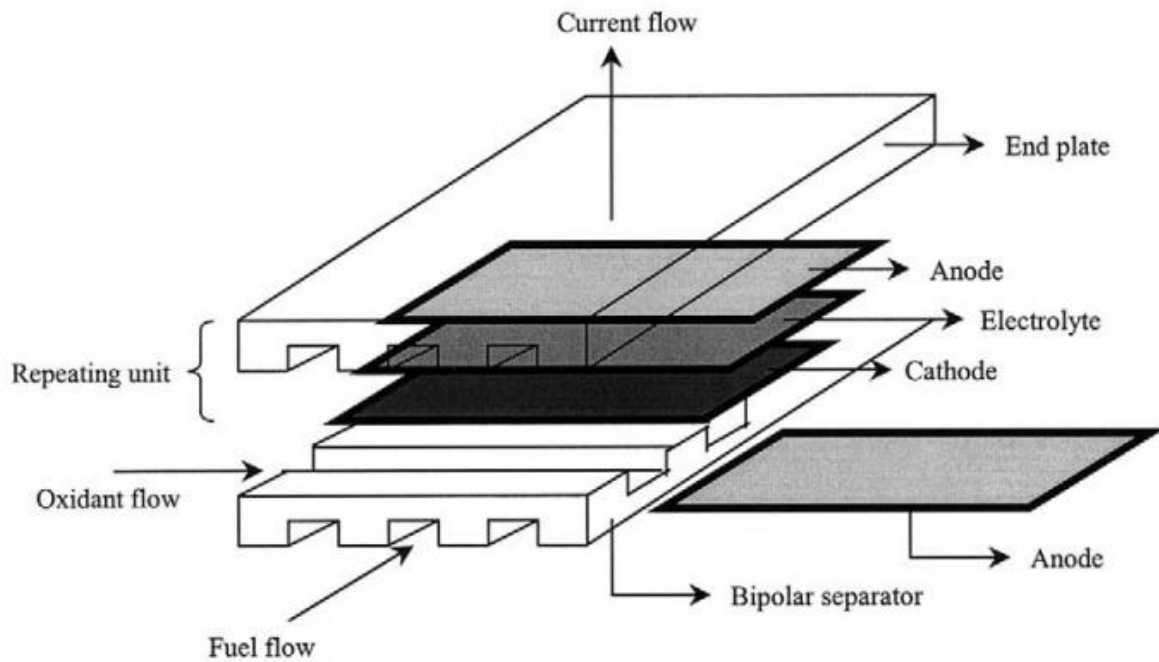


Figure 1.3 Typical planar SOFC configuration [1]

## 1.6 SOFC anode

Anode should facilitate the oxidation of fuel and transport of electrons from reaction site to current collector. It should also enable diffusion of gaseous fuel to the reaction sites and reaction products away from the reaction sites. Properties pertaining to structure, electricity, and electrochemistry have to be taken into consideration while choosing materials for anode. High temperature and intensive reducing atmosphere where anode has to operate, impose stringent criteria for anode material selection and give rise to special challenges concerning chemical stability and material degradation. To ensure electrode's satisfactory performance, anode materials should meet the following requirements [8]:

1. High electrocatalytic activity favoring oxidation of gaseous fuel
2. Predominant electronic conductivity permitting path of electrons
3. Thermal expansion coefficient (TEC) compatibility with adjacent components
4. Chemical compatibility with adjacent components
5. Continuous porous structure allowing rapid transport of gaseous fuel and reaction products in and out of the electrode

Porous Ni/YSZ (yttria-stabilized zirconia) cermet electrodes meet most of the abovementioned requirements, making them as ideal anodes for hydrogen-fed SOFCs [8]:

1. Ni serves as a competent electrocatalyst for electrochemical oxidation of  $H_2$ .
2. Ni conducts electrons with its satisfactory conductivity
3. Ni/YSZ anode is able to match adjoining components including YSZ electrolyte in terms of thermal expansion coefficient.
4. YSZ could inhibit the coarsening of Ni during operation.

5. YSZ provides a framework where Ni could be dispersed. Pores in between enable rapid transport of gaseous fuel and reaction products.

## 1.7 TPB-based kinetics in SOFC anode

Ni-YSZ cermet is one of the most prevailing anode materials for SOFC. In fact, physicochemical processes taking place within such an anode are very complicated, involving highly coupled catalytic and electrochemical reactions and transport phenomena. Obtaining a good understanding of such physicochemical mechanisms is one of the prerequisites to anode's optimization such as voltage loss mitigation. Considering that direct measurement of electrochemical reactions in porous structure is very difficult, developing an accurate model describing such physicochemical processes within anode is highly wanted [9].

In many past computational studies of the cermet anode, coupled with conservation equations representing gas transport and charge migration, a global electrochemical reaction expressed by Butler-Volmer equation is put forward, simplifying electrode reaction to a single step process [10][11][12]. Although such macro scale modelling generated results turning to be well-fitted with experimental outputs, it failed to present insights into intrinsic processes occurring within the anode. Accordingly, more fundamental modelling is anticipated to investigate the nature of anode reactions where parameters of interest such as triple-phase boundary length are specifically studied.

As demonstrated in Figure 1.4, a typical cermet anode consists of Ni particles for electronic conducting and YSZ particles for ionic conducting, with pores in between for transport of gaseous species. Within electrode, electrochemical reaction occurs in the vicinity of triple-phase boundary where Ni, YSZ, and pore interact. Triple-phase boundary length, as a parameter quantifying the electrochemically active region, influences electrochemical kinetics and anode performance [1]. Therefore, a quantitative knowledge of the TPB length is required to study electrochemical kinetics and anode performance.

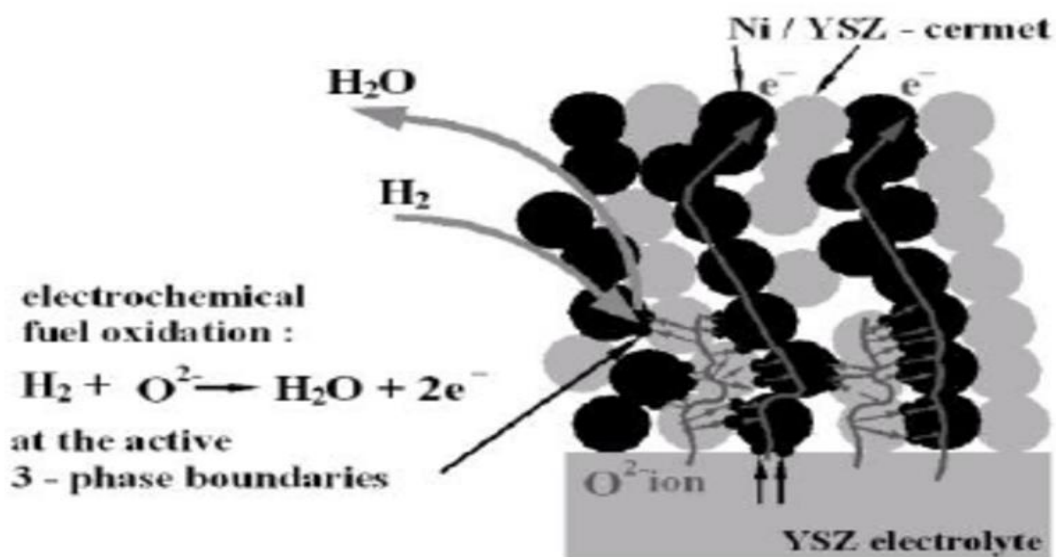


Figure 1.4 Ni/YSZ Anode of SOFC [13]

However, due to the complex microstructure of a Ni-YSZ cermet, quantification of the TPB length in such a 3D porous structure is technically inconvenient. In addition, the measurement of the TPB fraction actually participating in the reaction is also experimentally difficult. To circumvent such a dilemma, a Ni pattern anode is employed. The triple phase boundary length of a pattern anode is specified during the fabrication, enabling a study on TPB related electrochemical oxidation mechanism. Actually, an electrochemical reaction at the TPB is constituted by a sequence of elementary steps such as surface reactions and charge-transfer reactions. Through modelling pattern cell using an elementary kinetics approach, rate-limiting process is identified and TPB length effect is attempted to estimate. TPB-based kinetics assuming a rate-limiting step is then formulated, eligible to be applied to cermet anode as well. Such TPB-based kinetics lead to Butler-Volmer formulation representing the kinetics of rate-limiting step and overall electrode reaction. In that case, detailed electrochemical oxidation mechanism in anode is considered and described.

## **1.8 Thesis objective**

The overall objective of the thesis is to incorporate the TPB-based kinetics, derived from the pattern anode experiment, in a CFD model to evaluate the performance of Ni/YSZ cermet-based cells, with insights into intrinsic processes occurring within the anode presented. Such a model is expected to describe the species transport in the anode microstructure, in the gas phase and at the surface. Polarization curves, which typically characterize the cell performance, are simulated where TPB length as a fitting parameter is tuned to enable the agreement between simulation and experimental curves. Overpotential breakdown and species distribution are then investigated. Effects of operating temperature on SOFC is further studied.

## **1.9 Thesis outline**

Chapter 2 presents the theoretical background of the modelling work and subsequent validation and analysis. The literatures cover TPB based kinetics to be incorporated into modelling work and cell polarization behavior to be employed in model validation & performance analysis. Chapter 3 provides formulas and equations concerning charge transport, species/mass transport and momentum transport. Implementation of TPB based kinetics in electrochemistry modelling is highlighted. Chapter 4 offers polarization resulting from a validated model. Starting from that, overpotential breakdown and species distribution are then investigated. In addition, the operating temperature is tuned to study its effects on cell performance. Chapter 5 draws the conclusion of the report and projects the outlook for future research.

# 2

## Literature Survey

### 2.1 Polarization behavior

An operating SOFC outputs cell current at given cell voltage. It's necessary to evaluate SOFC performance quantitatively by current – voltage figure. At any stationary state, a single given voltage leads to a single current.

When electrodes are not electrically connected, no net current can be detected and an open circuit voltage would be measured. Once electrodes are electrically connected, the cell voltage turns to be lower than open circuit voltage. Such drop is attributed to irreversible losses like (1) activation overpotential, (2) Ohmic overpotential, and (3) concentration overpotential.

#### 2.3.1 Activation overpotential

The activation overpotential originates from slowness of reaction occurring at electrode. When evaluating overall rate of a reversible reaction, the rates of both forward and reverse directions should be considered. The net rate is given by the difference between the forward and reverse reaction rates. For example, the second charge transfer reaction at anode (Reaction 4) concerns forward and reverse reactions.

Forward reaction  $H(Ni) + OH^-(YSZ) \rightarrow (Ni) + H_2O(YSZ) + e^-(Ni)$

Reverse reaction  $(Ni) + H_2O(YSZ) + e^-(Ni) \rightarrow H(Ni) + OH^-(YSZ)$

Assuming  $J_f$  as the forward reaction rate and  $J_r$  as the reverse reaction rate, the net reaction rate is  $J_{net} = J_f - J_r$

Current density  $i$  and reaction rate  $J$  are related by  $i = nFJ$ . Similarly, net current density  $i_{net}$  is the difference between the current density of forward reaction  $i_f$  and the current density of reverse reaction  $i_r$ .

$$i_{net} = i_f - i_r$$

In more details

$$i_f = i^o e^{\alpha_a n F \eta_{act} / RT}$$

$$i_r = i^o e^{-\alpha_c n F \eta_{act} / RT}$$

In equilibrium, forward and reverse reaction rates must balance. In that case, activation overpotential is zero, making both forward and reverse current densities equal exchange current density, leading to zero net current density. If such dynamic balance is tipped, positive activation overpotential would favor anodic reaction, leading to non-zero net current density. It's easy to tell that higher activation overpotential leads to higher net current density, assuming exchange current density to be a constant.

Since Butler-Volmer equation must be solved implicitly for activation overpotential, several explicit approximations have been raised [14]. The formula of approximation varies depending on current density range.

$$\text{High current density field } \eta_{act} = \frac{RT}{\alpha_a n F} \ln\left(\frac{i}{i^o}\right) \quad \left(\frac{i}{i^o} > 4\right)$$

$$\text{Mid current density field } \eta_{act} = \frac{RT}{\alpha_a n F} \sinh^{-1}\left(\frac{i}{2i^o}\right) \quad (1 < \frac{i}{i^o} < 4)$$

$$\text{Low current density field } \eta_{act} = \frac{RT}{\alpha_a n F} \left(\frac{i}{i^o}\right) \quad \left(\frac{i}{i^o} < 1\right)$$

### 2.3.2 Ohmic overpotential

Due to resistance to electronic flow at electrodes and resistance to ionic flow within electrolyte, the cell voltage would drop as long as there is net current passing through the cell. Assuming cell resistance to be a constant, when current climbs up, Ohmic overpotential would consequently increase linearly.

$$\eta_{ohm} = i_a R_{ohm}$$

Considering most of the Ohmic overpotential is attributed to ionic resistance exerted by electrolyte [15], Ohmic overpotential could be estimated as the potential difference between electrolyte interfaces.

### 2.3.3 Concentration overpotential

Concentration overpotential is attributed to electrochemical reaction causing reactant depletion and product generation at TPB site. Such loss in reversible cell voltage can be predicted by Nernst equation [16].

$$\eta_{con} = \frac{RT}{nF} \ln\left(\prod_k \frac{p_k^{b\nu_k}}{p_k^{TPB\nu_k}}\right)$$

$p_k^b$  is the partial pressure of species  $k$  in bulk phase

$p_k^{TPB}$  is the partial pressure of species  $k$  at TPB site

For the SOFC studied, hydrogen is injected to the anode and air is injected to the cathode. The concentration overpotentials of anode and cathode could be figured out respectively.

$$\eta_{con,a} = \frac{RT}{2F} \ln\left(\frac{p_{H_2}^b}{p_{H_2}^{TPB}} \cdot \frac{p_{H_2O}^{TPB}}{p_{H_2O}^b}\right)$$

$$\eta_{con,c} = \frac{RT}{4F} \ln\left(\frac{p_{O_2}^b}{p_{O_2}^{TPB}}\right)$$

$\eta_{con,a}$  is the concentration overpotential in the anode

$\eta_{con,c}$  is the concentration overpotential in the cathode

## 2.2 Hydrogen oxidation at Ni/YSZ anode

SOFC operates on electrochemical reactions occurring at electrodes. The nature of oxidation occurring at anode lies in the charge transfer processes. Together with hydrogen adsorption/desorption and incorporation of oxygen ions between electrolyte surface and electrolyte bulk, charge transfer processes constitute a half-cell reaction. Among those elementary steps, a certain reaction is assumed to be rate-limiting, dictating the reaction rate of the overall oxidation reaction. The anode half-cell reaction can be globally formulated as:



$O_O^X$  is lattice oxygen

$V_O''$  is oxygen vacancy in electrolyte bulk

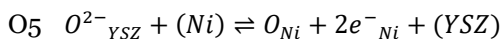
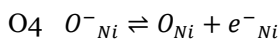
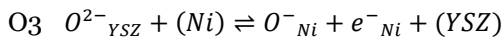
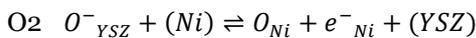
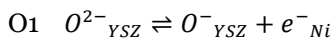
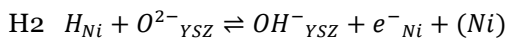
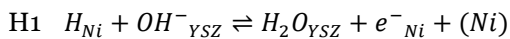
Notations in brackets are short for gas, electrolyte and anode respectively, standing for phases in which the relevant species exist.

### 2.2.1 Charge-transfer mechanisms

In Vogler's paper [17], a modelling study of hydrogen oxidation at Ni patterned anode is presented. Seven different charge transfer mechanisms are investigated via experimental data of patterned anode obtained by Bieberle [18] under a range of operating conditions.

Different scenarios picturing the actual pathway and nature of elementary step are proposed by Vogler [17]. The schematics in Figure 2.1 illustrate five different scenarios of elementary kinetics at Ni/YSZ TPB. The projected scenario (a) represents surface hydrogen spillover, involving Reaction H1 and Reaction H2. Reaction H1 depicts that a Ni-adsorbed hydrogen atom hopping to a hydroxyl ion on YSZ. Reaction H2 describes that a Ni-adsorbed hydrogen atom hopping to an oxygen ion on YSZ. The projected scenario (b) represents surface oxygen spillover, involving Reactions O1-O5. Reactions O1-O4 depicts that oxygen ions may hop from YSZ surface to Ni surface, undergoing two charge-transfer reactions that can take place before, after, or during the hop. Reaction O5 describes that oxygen ions may hop from YSZ surface to Ni surface, undergoing only one charge-transfer reaction that can take place during the hop. The projected scenario (c) represents surface hydroxyl spillover, involving Reaction OH which depicts that hydroxyl ion may hop from YSZ surface to Ni surface, undergoing only one charge-transfer reaction that can take place during the hop. The projected scenario (d) represents charge transfer by an interstitial hydrogen. The projected scenario (e) represents charge transfer on electrolyte surface only.

Abovementioned elementary reactions are formulated below.



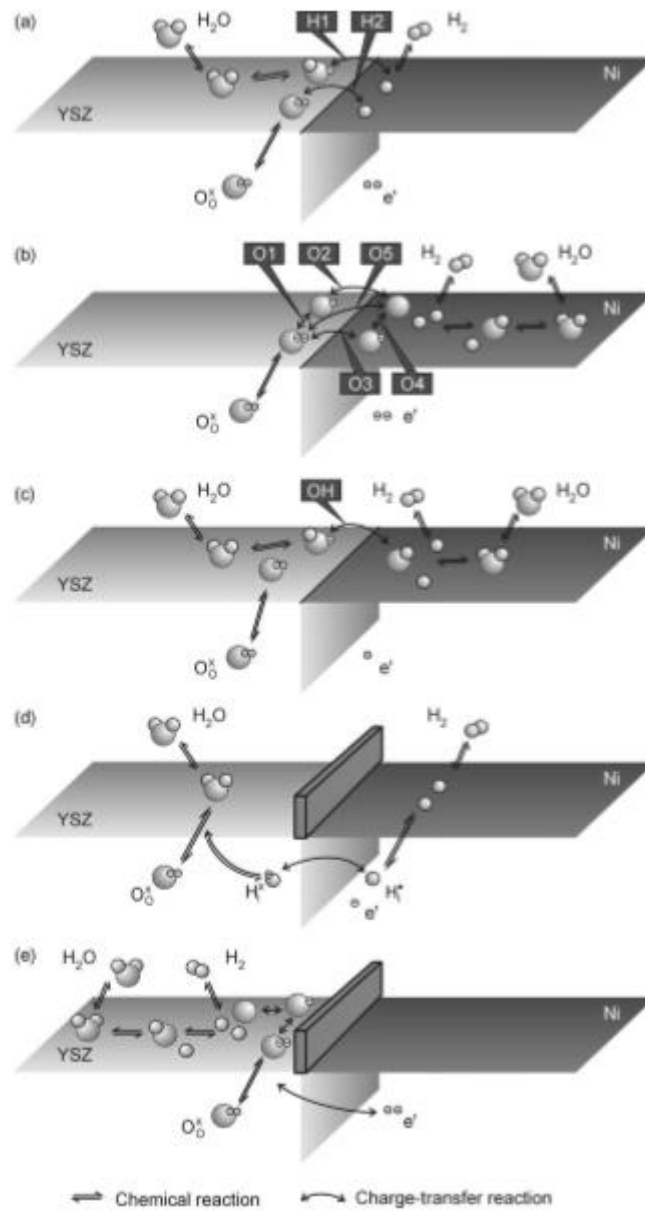
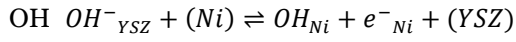


Figure 2.1 Elementary kinetics scenarios at Ni/YSZ TPB [17]

A total of seven different combinations of one or two elementary charge-transfer reactions, were referred as charge transfer mechanisms: two single hydrogen spillover mechanisms (H1 and H2), one double hydrogen spillover mechanism (H1+H2), three different oxygen spillover mechanisms (O1+O2, O3+O4 and O5), and one hydroxyl spillover mechanism (OH).

In Vogler's modelling study, polarization resistance and Tafel plot were simulated and compared to experimental data set under different operation conditions. Only one reaction mechanism was enabled at a time for trial simulation, while the other mechanisms were disabled. Ultimately, only the double hydrogen spillover mechanism, as shown in Figure 2.1 (a), turned to yield

agreement with the complete experimental data set. Consequently, the double hydrogen spillover from Ni to YSZ surface is reasonably considered as the dominant mechanism at anode [17].

### 2.1.2 Rate-limiting step

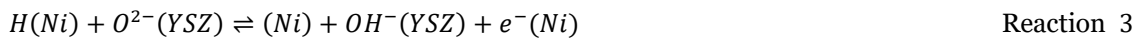
In Zhu's paper, a numerical framework of modelling chemically reacting flow in anode-supported SOFC is presented [19]. The model is capable of representing elementary heterogeneous chemical kinetics in form of multistep reaction mechanisms. A modified Butler-Volmer expression originating from elementary reactions depicts the charge-transfer chemistry, assuming a single rate-limiting step.

A detailed mechanism involving 5 elementary reactions at Ni-YSZ TPB is proposed.

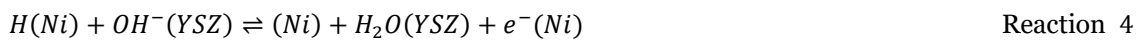
Adsorption/desorption of  $H_2$  on Ni surface



First charge-transfer reaction at TPB site (the same as Reaction H2)



Second charge-transfer reaction at TPB site (the same as Reaction H1)



Desorption/adsorption of  $H_2O$  on YSZ surface



Transfer of oxygen ions between surface YSZ and bulk YSZ



On the surface of Ni, 1 gaseous hydrogen molecule is adsorbed, split into 2 hydrogen atoms, with 2 empty Ni surface sites occupied. Later, 1 of the adsorbed hydrogen atoms reacts with 1 oxygen ion on YSZ surface, liberating 1 free electron at Ni, with 1 empty Ni surface site spared and 1 hydroxide ion on YSZ surface formed. Subsequently, the other produced hydrogen atom reacts with just-produced hydroxide ion on YSZ surface, releasing another free electron at Ni, with another empty Ni surface site spared and 1 vapor molecule on YSZ surface formed. And then, the produced vapor molecule gets desorbed from YSZ surface, resulting in 1 gaseous vapor molecule and 1 empty YSZ surface site. Finally, 1 lattice oxygen within YSZ bulk possesses 1 empty YSZ surface site, generating 1 oxygen ion on YSZ surface and 1 oxygen vacancy within bulk YSZ.

The abovementioned five elementary reactions involve six surface species and two gaseous species. The site fractions of adsorbed H and empty Ni must sum to unity. And the site fractions of oxygen ion, hydroxyl ion, vapor and empty YSZ must add up to unity as well.

$$\theta_H + \theta_{Ni} = 1 \quad \text{Equation 2.1}$$

$$\theta_O + \theta_{OH} + \theta_{H_2O} + \theta_{YSZ} = 1 \quad \text{Equation 2.2}$$

In Zhu's paper, the second charge-transfer reaction (Reaction 4) is assumed to be the rate-limiting one. Consequently, the other 4 reactions are assumed to be in equilibrium. Consequently, relevant surface coverages and partial pressures can be linked via equilibrium

constants of the 4 reactions in equilibrium.

$$\frac{\theta_H^2}{\theta_{Ni}^2 \frac{p_{H_2}}{p_0}} = K_2 \quad \text{Equation 2.3}$$

$$\frac{\theta_{Ni} \theta_{OH}}{\theta_H \theta_O} = K_3 \exp\left(\frac{F\Delta E_{a/e}}{RT}\right) \quad \text{Equation 2.4}$$

$$\frac{\theta_{YSZ} \left(\frac{p_{H_2O}}{p_0}\right)}{\theta_{H_2O}} = K_5 \quad \text{Equation 2.5}$$

$$\frac{\theta_O}{\theta_{YSZ}} = K_6 \quad \text{Equation 2.6}$$

Coupling Equations 2.1 – 2.6, species surface coverages could be sorted out respectively:

$$\theta_H = \frac{\sqrt{K_2 \frac{p_{H_2}}{p_0}}}{1 + \sqrt{K_2 \frac{p_{H_2}}{p_0}}} \quad \text{Equation 2.7}$$

$$\theta_{Ni} = \frac{1}{1 + \sqrt{K_2 \frac{p_{H_2}}{p_0}}} \quad \text{Equation 2.8}$$

$$\theta_{H_2O} = \frac{\left(\frac{p_{H_2O}}{p_0}\right)}{\left(\frac{p_{H_2O}}{p_0}\right) + K_5 + K_5 K_6 + \frac{\theta_H}{\theta_{Ni}} K_3 K_5 K_6 \exp\left(\frac{F\Delta E_{a/e}}{RT}\right)} \quad \text{Equation 2.9}$$

$$\theta_{YSZ} = \frac{K_5}{\left(\frac{p_{H_2O}}{p_0}\right) + K_5 + K_5 K_6 + \frac{\theta_H}{\theta_{Ni}} K_3 K_5 K_6 \exp\left(\frac{F\Delta E_{a/e}}{RT}\right)} \quad \text{Equation 2.10}$$

$$\theta_O = \frac{K_5 K_6}{\left(\frac{p_{H_2O}}{p_0}\right) + K_5 + K_5 K_6 + \frac{\theta_H}{\theta_{Ni}} K_3 K_5 K_6 \exp\left(\frac{F\Delta E_{a/e}}{RT}\right)} \quad \text{Equation 2.11}$$

$$\theta_{OH} = \frac{\frac{\theta_H}{\theta_{Ni}} K_3 K_5 K_6 \exp\left(\frac{F\Delta E_{a/e}}{RT}\right)}{\left(\frac{p_{H_2O}}{p_0}\right) + K_5 + K_5 K_6 + \frac{\theta_H}{\theta_{Ni}} K_3 K_5 K_6 \exp\left(\frac{F\Delta E_{a/e}}{RT}\right)} \quad \text{Equation 2.12}$$

The area-specific current density of the rate-limiting reaction can be written in elementary form.

$$i_{a,a_4} = l_{a,TPB} F [k_{f,a_4} \theta_H \theta_{OH} \exp\left(\frac{(\beta_{a,a_4} F \Delta E_{a/e})}{RT}\right) - k_{r,a_4} \theta_{H_2O} \theta_{Ni} \exp\left(-\frac{\beta_{c,a_4} F \Delta E_{a/e}}{RT}\right)] \quad \text{Equation 2.13}$$

$i_{a,a_4}$  is the area-specific current of Reaction 4

$k_{f,a_4}$  is the reaction rate constant of the forward reaction of Reaction 4

$k_{r,a_4}$  is the reaction rate constant of the reverse reaction of Reaction 4

$\beta_{a,a_4}$  is the anodic symmetric factor of Reaction 4 in the anode

$\beta_{c,a_4}$  is the cathodic symmetric factor of Reaction 4 in the anode

Substituting Equations 2.7 – 2.12 into Equation 2.13, a more compact Butler-Volmer form is presented.

$$i_{a,a_4} = i_{a,a_4}^0 \left[ \exp\left(\frac{(\beta_{a,a_4} + 1) F \eta_{act,a}}{RT}\right) - \exp\left(-\frac{\beta_{c,a_4} F \eta_{act,a}}{RT}\right) \right] \quad \text{Equation 2.14}$$

$i_{a,a_4}^0$  is the area-specific exchange current of Reaction 4

$$i_{a,a_4}^0 = l_{a,TPB} F k_{r,a_4} (K_4 K_2 K_3 K_5 K_6)^{\beta_{c,a_4}/2} \left(\frac{p_{H_2}}{p_0}\right)^{\beta_{c,a_4}/2} \left(\frac{p_{H_2O}}{p_0}\right)^{1-\beta_{c,a_4}/2} \left\{ \left(1 + K_2^{\frac{1}{2}} \left(\frac{p_{H_2}}{p_0}\right)^{\frac{1}{2}}\right) \left[\left(\frac{p_{H_2O}}{p_0}\right) + K_5 + \right. \right.$$

$$K_5 K_6 + K_3 K_5 K_6 K_2^{\frac{1}{2}} \left( \frac{p_{H_2}}{p_0} \right)^{\frac{1}{2}} \exp\left(\frac{F \Delta E_{a/e}^{eq}}{RT}\right) \}}^{-1} \quad \text{Equation 2.15}$$

$$\eta_{act,a} = \Delta E_{a/e} - \Delta E_{a/e}^{eq} \quad \text{Equation 2.16}$$

$\eta_{act,a}$  is the anode activation overpotential

$\Delta E_{a/e}$  is the electric-potential difference between anode and electrolyte

$\Delta E_{a/e}^{eq}$  is the equilibrium electric-potential difference between anode and electrolyte

The Butler-Volmer equation can be simplified by assuming that YSZ surface is nearly fully covered by oxygen ions. In that case, the exchange current density of the rate-limiting step can be rewritten.

$$i_{a,a_4}^0 = l_{TPB} F k_{r,a_4} (K_4 K_3)^{\beta_{c,a_4}/2} \left( \frac{1}{K_5 K_6} \right)^{1-\beta_{c,a_4}/2} \frac{(K_2 \frac{p_{H_2}}{p_0})^{\beta_{c,a_4}/2} (\frac{p_{H_2} O}{p_0})^{1-\beta_{c,a_4}/2}}{1 + (K_2 \frac{p_{H_2}}{p_0})^{1/2}} \quad \text{Equation 2.17}$$

Actually, there are 2 charge-transfer reactions, with Reaction 4 assumed to be rate-limiting and Reaction 3 assumed to be in equilibrium. As a result, the area-specific current density in the anode is twice the area-specific current density of Reaction 4 [19].

$$i_{a,a} = 2i_{a,a_4} = 2i_{a,a_4}^0 \left[ \exp\left(\frac{(\beta_{a,a_4}+1)F\eta_{act,a}}{RT}\right) - \exp\left(-\frac{\beta_{c,a_4}F\eta_{act,a}}{RT}\right) \right] \quad \text{Equation 2.18}$$

$i_{a,a}$  is the area-specific current density in the anode

## 2.3 Oxygen reduction at cathode

According to Zhu [19], the area-specific current density in the cathode can be expressed in Butler-Volmer form.

$$i_{a,c} = i_{a,c}^0 \left[ \exp\left(\frac{\beta_{a,c} F \eta_{act,c}}{RT}\right) - \exp\left(-\frac{\beta_{c,c} F \eta_{act,c}}{RT}\right) \right] \quad \text{Equation 2.19}$$

$i_{a,c}$  is the area-specific current density in the cathode

$i_{a,c}^0$  is the exchange current density in the cathode

$\beta_{a,c}$  is the anodic symmetric factor of the cathode reaction

$\beta_{c,c}$  is the cathodic symmetric factor of the cathode reaction

$\eta_{act,c}$  is the cathode activation overpotential

$$i_{a,c}^0 = i_{O_2}^* \frac{(p_{O_2}/p_{O_2}^*)^{1/4}}{1 + (p_{O_2}/p_{O_2}^*)^{1/2}} \quad \text{Equation 2.20}$$

$i_{a,O_2}^*$  is used as an empirical parameter to fit experimental observation

According to Zhu,  $i_{a,O_2}^* = 2.8 \text{ A/cm}^2$  is obtained [19].

According to Matsuzaki and Yasuda,  $p_{O_2}^* = 0.090273 \text{ atm}$  is obtained [20].

## 2.4 TPB length in anode

State of the art fuel cell electrodes typically have a complex microstructure involving interconnected electronically and ionically conducting phases, gas-phase porosity. Determining such microstructure is a critical yet missing link between material properties and performance of electrode. To obtain a detailed 3D understanding of the microstructure, a 3D microstructure reconstruction could be conducted [21]. With the help of focused ion beam technique, a trench

into a cross-sectional surface in the vicinity of anode is milled. Subsequent scanning electron microscopy generates a series of consecutive images which could be stacked in 3D space later on. Through such 3D reconstruction process, TPB length and percolated TPB portion feasible to contribute to electrochemistry are revealed. TPB length, widely viewed as a critical geometrical parameter of electrode, is expected to influence reaction rate. For effective TPB sites contiguously accessing the rest of microstructure, connections of pore to gas flow via neighboring pore network, nickel phase to external circuit via nickel network, and YSZ phase to bulk electrolyte via YSZ network are all ensured. What's more, of such percolated portion, only a tiny fraction which is located in a small depth from electrolyte/electrode interface actually participates in the electrochemical reaction, forming an electrochemically active thickness [22].

# 3

## Model Development

### 3.1 Purposes and assumptions

A model with high fidelity is expected to be created in Comsol possessing multi-physics. The model should resemble experimental sample tested by Jiang [25]. The simulated polarization curves are compared to the experimental ones for validation.

To simplify the modelling work, some assumptions are made ahead of model development:

1. The gases within both electrodes and channels are ideal.
2. The gaseous flows within both electrodes and channels are Laminar ones.
3. The cell is operated in a steady state.
4. The cell has a homogeneous temperature.
5. TPB length and specific active area are both homogeneous microstructural properties of anode, assuming TPB sites are homogeneously distributed at anode.

### 3.2 Geometry and materials

In Jiang's experiment [25], the cell was fixed at a test rig where Ni-YSZ anode is exposed to fuel gas injected upwards through alumina tube and cathode was exposed to air flow injected downwards from the top, as illustrated in Figure 3.1. Surrounded by furnace, the cell was heated to a desired operating temperature. Operating pressure was specified as 1 atm.

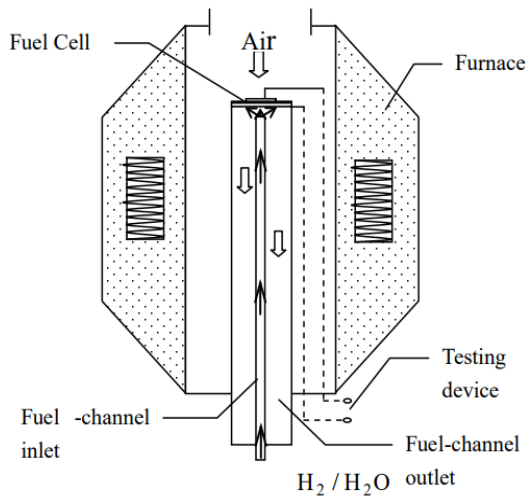


Figure 3.1 Experimental testing system [26]

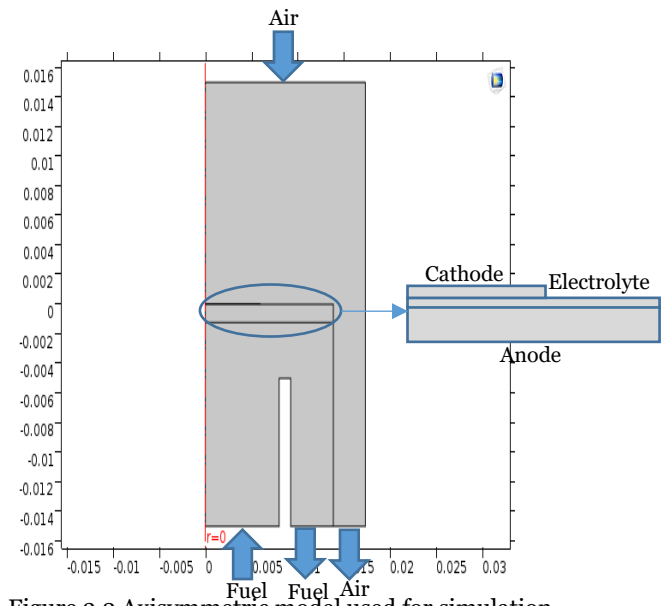


Figure 3.2 Axisymmetric model used for simulation

A 2D axisymmetric model (Figure 3.2) is developed in Comsol, consisting of 2 gas channels, 2 electrodes and 1 electrolyte. When sweeping around its symmetric axis (indicated in red where  $r = 0$ ), such 2D axisymmetric model is converted to the 3D geometry of experimental set-up.

Ni-YSZ anode was prepared from NiO and YSZ powders [25]. Raw powders were premixed in a certain composition of 55% volume fraction of NiO and 45% volume fraction of YSZ. After successive processes of ball-milling, drying and screening, raw materials turned to a circular disk shape which was further die-pressed and pre-sintered. Subsequently, the disk was coated with a thin layer of NiO-YSZ after firing treatment. Finally, NiO/YSZ was reduced in  $N_2+H_2$  atmosphere at cell operating temperature before electrochemical characterization.

### 3.3 Multiphysics modelling

The SOFC model should involve charge transport, species/mass transport and momentum transport, corresponding to charge balance, mass balance, and momentum balance, respectively. Accordingly, specific physics in the Comsol are selected to solve for relevant conservation equations.

Conforming to the charge conservation, electrochemical reaction kinetics, and electronic and ionic charge migration are presented in the physics of Secondary Current Distribution. The physics of Secondary Current Distribution deals with transport of charged ions in an electrolyte of uniform composition and current conduction at electrodes using Ohm's law in combination with a charge balance. In addition, the physics accounts for activation overpotential, which is linked to the electrochemical rate of the charge transfer reaction current via Butler-Volmer equation.

Abiding by mass conservation, multicomponent gaseous species transport in gas channels and porous electrodes is presented in the physics of Transport of Concentrated Species. The physics of Concentrated Species Transport is used to study fluid mixtures where the species concentrations are of the same order of

magnitude. In that case, properties of the mixture depend on the composition. The molecular/ionic interactions among all species need to be considered as well. The physics includes model for multicomponent diffusion, where the diffusive driving force of each species depends on the mixture composition, temperature, and pressure.

Complying with mass and momentum balance, gas flow distribution in gas channels and porous electrodes is presented in the physics of Free and Porous Media Flow and categorized to computational fluid dynamics. The physics of Free and Porous Media Flow is used to compute velocity and pressure fields of single phase flow where free flow is connected to porous media. The physics is used over at least two different domains: a free channel and a porous medium.

Together with governing equations in physics, relevant initial conditions and boundary conditions are specified considering they are indispensable when solving problems. Boundary conditions provide a set of constraints when exploring a specific solution. Initial values offer a guess for some quantity to initiate the iterative study.

### 3.3.1 Electrochemistry

The modelling of electrochemistry aims to relate electrical variables (i.e. current and voltage) and chemical ones (i.e. species partial pressure). To approach such target, it is essential to apply governing equations presenting a reasonable description of electrochemical phenomena taking place in a fuel cell.

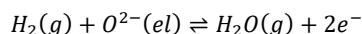
When fuel is supplied to the anode and oxidant is supplied to the cathode, a potential difference arises between the electrodes. If the electrodes are not electrically connected and fuel-crossover is not taken into account, the potential difference would equal the electromotive force (also called open circuit voltage) resulting from the redox reactions. In addition, open circuit voltage (OCV) represents the maximum potential difference provided by the cell at given conditions. When current is drawn from the cell, the potential difference between the electrodes decreases.

In the following sections, specific mathematical descriptions are provided for electrode potential difference, cell electrochemical reactions and charge transport.

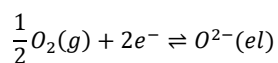
#### 3.3.1.1 Cell Voltage

The potential difference between electrodes is determined by redox reactions taking place at electrodes. A pair of half-cell reactions involve oxidation of fuel on the anode side and reduction of oxygen on the cathode side.

The half-cell hydrogen oxidation reaction is given by:



The half-cell oxygen reduction reaction is given by:



The reversible potential of the cell is defined as the difference between the equilibrium potentials of anode and cathode.

$$E_{rev} = E_c^{eq} - E_a^{eq} \quad \text{Equation 3.1}$$

$E_{rev}$  is the cell reversible potential

$E_a^{eq}$  is the anode equilibrium potential

$E_c^{eq}$  is the cathode equilibrium potential

As a function of Gibbs free energy of relevant reaction, the equilibrium potential depends on the temperature and activities of reactants and products. The equilibrium potential of single electrode is given by:

$$E^{eq} = \frac{1}{nF} [\Delta g^0 + RT \ln \prod_k a_k^{\nu_k}] \quad \text{Equation 3.2}$$

$E^{eq}$  is the equilibrium potential

$n$  is the number of participating electrons

$\Delta g^0$  is the molar standard state Gibbs free energy change

$a_k$  is the chemical activity of species  $k$

$\nu_k$  is the stoichiometric coefficient of species  $k$

Coupling anode and cathode reactions, equilibrium potential difference between electrodes leads to Nernst formulation of reversible potential:

$$E_{rev} = -\frac{\Delta g_{H_2-H_2O}^0}{2F} + \frac{RT}{2F} \ln\left(\frac{a_{H_2} a_{O_2}^{\frac{1}{2}}}{a_{H_2O}}\right) \quad \text{Equation 3.3}$$

$$a_{H_2} = \frac{p_{H_2}^b}{p_0} \quad \text{Equation 3.4}$$

$$a_{H_2O} = \frac{p_{H_2O}^b}{p_0} \quad \text{Equation 3.5}$$

$$a_{O_2} = \frac{p_{O_2}^b}{p_0} \quad \text{Equation 3.6}$$

$\Delta g_{H_2-H_2O}^0$  is the molar standard state Gibbs free energy change of the overall cell reaction

$p_k^b$  is the partial pressure of species  $k$  in bulk phase

In ideal case where fuel crossover or leakage is avoided, open circuit voltage equals cell equilibrium potential [27]. In the work, experimentally measured open circuit voltage is used.

Once the cell is connected to an electric load, activation overpotential, ohmic overpotential and concentration overpotential would cause a drop in cell voltage.

$$V_{cell} = OCV - \eta_{conc,a} - \eta_{conc,c} - \eta_{act,a} - |\eta_{act,c}| - \eta_{ohm} \quad \text{Equation 3.7}$$

$$\eta_{act,a} = \Delta E_{a/e} - \Delta E_{a/e}^{eq} \quad \text{Equation 3.8}$$

$$\eta_{act,c} = \Delta E_{c/e} - \Delta E_{c/e}^{eq} \quad \text{Equation 3.9}$$

$$\eta_{ohm} = i_{cell} R_{ohm} \quad \text{Equation 3.10}$$

$$\eta_{con,a} = \frac{RT}{2F} \ln\left(\frac{p_{H_2}^b}{p_{H_2}^{TPB}} \cdot \frac{p_{H_2O}^{TPB}}{p_{H_2O}^b}\right) \quad \text{Equation 3.11}$$

$$\eta_{con,c} = \frac{RT}{4F} \ln\left(\frac{p_{O_2}^b}{p_{O_2}^{TPB}}\right) \quad \text{Equation 3.12}$$

$V_{cell}$  is the cell voltage

$i_{cell}$  is the cell current density

$\Delta E_{a/e}^{eq}$  is the electric-potential difference between the anode and electrolyte

$\Delta E_{c/e}^{eq}$  is the electric-potential difference between the cathode and electrolyte

$p_k^{TPB}$  is the partial pressure of species  $k$  at TPB site

For the cell to be studied,  $V_{cell}$  is pre-defined and  $OCV$  is pre-determined. The overpotentials and the cell current density are unknowns. The activation overpotential is involved in the Butler-Volmer equation where it is linked to the cell current density. Since the electrolyte's resistance is constant, the Ohmic overpotential is linear to the cell current density. The concentration overpotential is defined as a function of the partial pressure of species in bulk phase and the partial pressure of species at TPB site, where those pressures are linked to the cell current density as well. The overpotentials and the cell current density are iteratively solved for by Comsol at every stationary state.

### 3.3.1.2 Electrochemical Reactions

For a TPB to contribute to anode electrochemistry, the gaseous, ionic, and electronic phases adjoining the TPB must have a contiguous connection to the rest of the microstructure.

It is assumed by Vogler [17] that processes occurring at the TPB sites are made up of complicated physiochemical phenomena, including adsorption/desorption of  $H_2$  molecules on/from Ni, charge-transfer reactions, desorption/adsorption of  $H_2O$  molecules from/on YSZ and transfer of oxygen ions between surface and bulk YSZ.

It is assumed by Zhu [19] that one charge-transfer reaction is the slowest step of the entire reaction scheme. So the rate of the electrochemical oxidation can be determined by the rate of such limiting step.

The area-specific current density of the rate-limiting reaction (Reaction 4) can be written in Butler-Volmer form [19].

$$i_{a,a_4} = i_{a,a_4}^0 \left[ \exp\left(\frac{(\beta_{a,a_4}+1)F\eta_{act,a}}{RT}\right) - \exp\left(-\frac{\beta_{c,a_4}F\eta_{act,a}}{RT}\right) \right] \quad \text{Equation 3.13}$$

$i_{a,a_4}$  is the area-specific current of Reaction 4 in the anode

$i_{a,a_4}^0$  is the area-specific exchange current of Reaction 4 in the anode

$\beta_{a,a_4}$  is the anodic symmetric factor of Reaction 4 in the anode

$\beta_{c,a_4}$  is the cathodic symmetric factor of Reaction 4 in the anode

According to Tabish's report,  $\beta_{a,a_4} = 0.3$  and  $\beta_{c,a_4} = 0.7$

$\eta_{act,a}$  is the activation overpotential in the anode

There are 2 charge-transfer reactions, with Reaction 4  $H(Ni) + OH^-(YSZ) \rightleftharpoons (Ni) + H_2O(YSZ) + e^-(Ni)$  assumed to be rate-limiting and Reaction 3  $H(Ni) + O^{2-}(YSZ) \rightleftharpoons (Ni) + OH^-(YSZ) + e^-(Ni)$  assumed to be in equilibrium. Thus, the overall current density is twice the current density resulting from Reaction 4 [19].

$$i_{a,a} = 2i_{a,a_4} = 2i_{a,a_4}^0 \left[ \exp\left(\frac{(\beta_{a,a_4}+1)F\eta_{act,a}}{RT}\right) - \exp\left(-\frac{\beta_{c,a_4}F\eta_{act,a}}{RT}\right) \right] \quad \text{Equation 3.14}$$

$i_{a,a}$  is the area-specific current in the anode

Dependent on partial pressure of gaseous species as well, area-specific exchange current in the anode is fully defined as a function of area-specific TPB length [19]. Divided by area-specific TPB length, the area-specific exchange current is converted to TPB length-specific exchange current.

$$i_{a,a}^0 = 2l_{a,TPB} F k_{r,a_4} (K_4 K_3)^{\beta_{c,a_4/2}} \left(\frac{1}{K_5 K_6}\right)^{1-\beta_{c,a_4/2}} \frac{(K_2 \frac{p_{H_2}}{p_0})^{\beta_{c,a_4/2}} (\frac{p_{H_2O}}{p_0})^{1-\beta_{c,a_4/2}}}{1+(K_2 \frac{p_{H_2}}{p_0})^{1/2}} \quad \text{Equation 3.15}$$

$$i_{i,a}^0 = \frac{i_{a,a}^0}{l_{a,TPB}} = 2F k_{r,a_4} (K_4 K_3)^{\beta_{c,a_4/2}} \left(\frac{1}{K_5 K_6}\right)^{1-\beta_{c,a_4/2}} \frac{(K_2 \frac{p_{H_2}}{p_0})^{\beta_{c,a_4/2}} (\frac{p_{H_2O}}{p_0})^{1-\beta_{c,a_4/2}}}{1+(K_2 \frac{p_{H_2}}{p_0})^{1/2}} \quad \text{Equation 3.16}$$

$$k_{r,a_4} = k_{a_4}^0 \exp\left(-\frac{E_{ct}^{act}}{RT}\right) / K_4 \quad \text{Equation 3.17}$$

$$K_i = e^{-\frac{\Delta g_i}{RT}} \quad \text{Equation 3.18}$$

$$\Delta g_i = \Delta h_i - T \Delta s_i \quad \text{Equation 3.19}$$

$i_{a,a}^0$  is the area-specific exchange current of the anode

$i_{i,a}^0$  is the TPB length-specific exchange current of the anode

$l_{a,TPB}$  is the area-specific TPB length

$k_{r,a_4}$  is the reverse reaction rate of Reaction 4 in the anode

$K_i$  is the equilibrium constant of Reaction  $i$  in the anode

$k_{a_4}^0$  is the pre-exponential factor of the forward direction of Reaction 4

According to Tabish's report,  $k_{a_4}^0 = 15 \frac{mol}{cm \cdot s}$  is obtained

$E_{ct}^{act}$  is the activation energy of the forward direction of Reaction 4

According to Patel's report,  $E_{ct}^{act} = 1.31 eV$  is obtained [23]

$\Delta g_i$  is the molar Gibbs free energy change in Reaction  $i$

$\Delta h_i$  is the molar enthalpy change in Reaction  $i$

$\Delta s_i$  is the molar entropy change in Reaction  $i$

The equilibrium constant of each reaction can be calculated from the thermodynamic data provided by Connor [28] and Vogler [17].

Species	$h$ (kJ/mol)	$s$ ( $\frac{J}{K \cdot mol}$ )
$H_2O$ (g) [28]	-212.8	235.5
$H_2$ (g) [28]	22.9	168.3
$H$ (Ni) [28]	-31.2	41.1
$OH^-$ (YSZ) [17]	-283	67
$O^{2-}$ (YSZ) [17]	-236	0
$H_2O$ (YSZ) [17]	-273	98
$O_s^{2-}$ (YSZ) [17]	-236	0

Table 3.1 Thermodynamic data of relevant species

Multiplied with effective volume-specific TPB length in cermet anode, the TPB length-specific exchange current is converted to volume-specific exchange current density in anode. Furthermore, divided by active specific area which represents the amount of catalytic active area (the area of Ni for Ni-YSZ cermet anode)

per unit volume of electrode, the volume-specific exchange current density is converted to area-specific exchange current density.

$$i_{v,a}^0 = i_{l,a}^0(\phi l_{v,TPB}) \quad \text{Equation 3.20}$$

$$i_{a,a}^0 = \frac{i_{v,a}^0}{a_v} = 2Fk_{r,a_4}(K_4K_3)^{\frac{\beta_{c,a_4}}{2}} \left(\frac{1}{K_5K_6}\right)^{1-\frac{\beta_{c,a_4}}{2}} \frac{\left(K_2\frac{p_{H_2}}{p_0}\right)^{\frac{\beta_{c,a_4}}{2}} \left(\frac{p_{H_2O}}{p_0}\right)^{1-\frac{\beta_{c,a_4}}{2}}}{1+\left(K_2\frac{p_{H_2}}{p_0}\right)^{\frac{1}{2}}} (\phi l_{v,TPB})/a_v \quad \text{Equation 3.21}$$

$l_{v,TPB}$  is the physical volume-specific TPB length in the anode

$\phi$  is the active portion of volume-specific TPB length in the anode

$\phi l_{v,TPB}$  is the effective volume-specific TPB length in the anode which quantifies the TPBs actually participating in the electrochemical reaction

$a_v$  is the active specific area

According to Zhu's paper,  $a_v = 1080 \text{ cm}^2/\text{cm}^3$

### 3.3.1.3 Charge Transport and Conservation

The charge transport within SOFC can be realized within electronic conducting media like Ni and ionic conducting media like YSZ. Charge movement is governed by the potential difference across electrodes. Charge flux, termed as current density as well, is given by Ohm's law:

$$i = -\sigma \nabla E \quad \text{Equation 3.22}$$

$i$  is the area-specific current density

$\sigma$  is the conductivity

$E$  is the potential

In addition, charge conservation is depicted.

$$\nabla i = Q \quad \text{Equation 3.23}$$

$Q$  is the volumetric charge source term

$Q$  is nonzero only in the reactive region where charge transfer occurs

### 3.3.1.4 Initial values

Over the domains of electrolyte and anode, electrolyte potential and electric potential are both preset as zero. Over the domain of cathode, electrolyte potential is preset as zero while electric potential is set as cell voltage.

### 3.3.1.5 Boundary condition

The upper side of cathode is maintained at cell voltage which is assigned manually before simulation. The lower side of anode is grounded.

## 3.3.2 Computational fluid dynamics -- Species transport

Maxwell-Stefan diffusion model with convection, as transport mechanism, is selected for the physics of

Transport of Concentrated Species. This option employs the most detailed diffusion model, requiring that all the binary diffusivities of all component pairs are known.

### 3.3.2.1 Species conservation

This section solves for mass fractions of species. The basic equation for the transport of species  $i$  takes diffusion, convection and chemical reaction into account.

$$\nabla \cdot (\rho \omega_i \mathbf{u}) = -\nabla \cdot \mathbf{j}_i + R_i \quad \text{Equation 3.24}$$

$\nabla \cdot (\rho \omega_i \mathbf{u})$  is the convection term

$\rho$  is the density

$\omega_i$  is the mass fraction of species  $i$

$\mathbf{u}$  is the velocity

$\nabla \cdot \mathbf{j}_i$  is the diffusion term

$\mathbf{j}_i$  is the mass flux of species  $i$

$R_i$  is the chemical mass source term of species  $i$

$R_i$  is linked to electrode current density via coupling with electrochemistry interface in later section

Considering that the Maxwell-Stefan model is selected to employ the species diffusion, abovementioned mass flux can be written as [29].

$$\mathbf{j}_i = -\rho \omega_i \sum_k D_{ik,eff} \left( \frac{M}{M_k} \left( \nabla \omega_k + \omega_k \frac{\nabla M}{M} \right) + (x_k - \omega_k) \frac{\nabla P}{P} \right) \quad \text{Equation 3.25}$$

$$M = \sum_k x_k M_k \quad \text{Equation 3.26}$$

$$\rho = \frac{PM}{RT} \quad \text{Equation 3.27}$$

$D_{ik,eff}$  is the effective binary diffusivity of species  $i$  and  $k$

$M$  is the averaged molar mass

$M_k$  is the molar mass of species  $k$

$x_k$  is the molar fraction of species  $k$

### 3.3.2.2 Extended Maxwell-Stefan Model

On top of molecular diffusion, Knudsen diffusion within electrode should be considered as well, entailing an extended Maxwell-Stefan model [30]. Due to porosity and tortuosity in electrodes, diffusivity is normalized with these structural parameters.

Taking Knudsen diffusion and porous structure into account, effective binary diffusivity concerning species  $i$  and  $k$  is modified [31].

$$D_{ik,eff} = \frac{\varepsilon}{2\tau} \left[ \frac{1}{\frac{1}{D_{ik}} + \frac{1}{D_{iM}}} + \frac{1}{\frac{1}{D_{ik}} + \frac{1}{D_{kM}}} \right] \quad \text{Equation 3.28}$$

$\varepsilon$  is the porosity of electrode

$\tau$  is the tortuosity of electrode

$D_{ik}$  is the binary diffusivity of species  $i$  and species  $k$

$D_{i/kM}$  is the Knudsen diffusivity of species  $i/k$

Knudsen diffusivity is defined as a function of particle radius of electrode and molecular weight of diffusing species [30].

$$D_{i/kM} = \frac{2r_p}{3} \sqrt{\frac{8RT}{\pi M_{i/k}}} \quad \text{Equation 3.29}$$

$r_p$  is the pore radius of electrode

$M_{i/k}$  is the molar mass of species  $i/k$

According to Fuller-Schettler-Giddings method, binary molecular diffusivity is defined below [32].

$$D_{ik} = \frac{10^{-3} T^{1.75} \left( \frac{1}{M_i} + \frac{1}{M_k} \right)^{\frac{1}{2}}}{P \left[ (\sum V_i)^{\frac{1}{3}} + (\sum V_k)^{\frac{1}{3}} \right]^2} \quad \text{Equation 3.30}$$

$P$  is total pressure

$V_{i/k}$  is the diffusion volume of species  $i/k$

The diffusion volumes for relevant species are listed. [32]

Species	$H_2$	$H_2O$	$O_2$	$N_2$
Diffusion volume	7.07	12.7	16.6	17.9

Table 3.2 The diffusion volumes for relevant species

Based on extended Maxwell-Stefan model, the local intrinsic concentration of fuel reactant at site adjacent to TPB is evaluated. To take further step, fuel reactant concentration at TPB region is obtained by considering the surface diffusion as well [33]. Assume that species  $i$  is referred to as fuel reactant.

$$c_{i.TPB} = c_{i,b} - \left( \frac{D_{i,eff}}{D_{i,s}} \right)^{1-\theta_i} (c_{i,b} - c_i) \quad \text{Equation 3.31}$$

$c_{i.TPB}$  is the concentration of species  $i$  at TPB site

$c_{i,b}$  is the concentration of species  $i$  in bulk phase

$c_i$  is the local intrinsic concentration of species  $i$  at site adjacent to TPB

$D_{i,eff}$  is the effective diffusivity of species  $i$

$D_{i,s}$  is the surface diffusion coefficient of species  $i$

$\theta_i$  is the relative surface coverage of species  $i$

The involved effective diffusivity of species  $i$  is defined [31].

$$D_{i,eff} = \frac{\varepsilon}{\tau} \left( \frac{1}{D_{ik}} + \frac{1}{D_{iM}} \right) \quad \text{Equation 3.32}$$

The surface diffusion coefficient of species  $i$  is defined [30].

$$D_{i,s} = \frac{D_{i,s,0}^{1-\theta_i} D_{i,s,1}^{\theta_i}}{1-\theta_i} \quad \text{Equation 3.33}$$

$D_{i,s,0}$  is the surface diffusion coefficient of species  $i$  at zero coverage

$D_{i,s,1}$  is the surface diffusion coefficient of species  $i$  at full coverage

The relative surface coverage of species  $i$  is defined [30].

$$\theta_i = \frac{b_i p_i}{\sum_k b_k p_k} \quad \text{Equation 3.34}$$

$b_k$  is the Langmuir parameter of species  $k$

$p_k$  is the partial pressure of species  $k$

The parameters concerning surface diffusion at 800°C are listed [33]

Parameters	$D_{H_2,s,0}$	$D_{H_2,s,1}$	$b_{H_2}$	$b_{H_2O}$
Values	$4 \times 10^{-5} \text{ m}^2/\text{s}$	$4 \times 10^{-7} \text{ m}^2/\text{s}$	$2.858 \times 10^{-9} \text{ 1/Pa}$	$3.484 \times 10^{-8} \text{ 1/Pa}$

**Table 3.3 The extreme surface diffusivities and Langmuir parameters of the anode species**

### 3.3.2.3 Initial values

The initial molar fraction of oxygen over the domains of cathode and air channel is preset as  $x_{O_2}$ . The initial molar fraction of hydrogen over the domains of anode and fuel channel is preset as  $x_{H_2}$ .  $x_{O_2}$  is constantly equal to 0.21.  $x_{H_2}$  equals 0.85/0.50/0.20 when molar fraction of inlet hydrogen is 0.85/0.50/0.20.

### 3.3.2.4 Boundary condition

The molar fraction of oxygen at the inlet of air channel is fixed at  $x_{O_2}$  and the molar fraction of hydrogen at the inlet of fuel channel is maintained at  $x_{H_2}$ .  $x_{O_2}$  is constantly equal to 0.21.  $x_{H_2}$  equals 0.85/0.50/0.20 when molar fraction of inlet hydrogen is 0.85/0.50/0.20.

### 3.3.2.5 Coupling

A mass source linked to electrode current density in an electrochemistry interface is defined.

$$R_i = \frac{\nu_i i_v}{nF} M_i \quad \text{Equation 3.35}$$

$R_i$  is the chemical mass source of species  $i$

$\nu_i$  is the stoichiometric coefficient of species  $i$

$i_v$  is the volume-specific current density

$n$  is the number of electrons

$M_i$  is the molar mass of species  $i$

## 3.3.3 Computational fluid dynamics – Gas flow distribution

Compressible flow ( $Ma < 0.3$ ), as the most general case for compressibility of isothermal flow, is selected for the physics of Free and Porous Flow. This option makes no assumptions for the system that is being solved. Any dependency that the fluid properties may have on the variables is considered. In this case, any kind of flow including incompressible flow can be modelled and described [34].

### 3.3.3.1 Mass conservation

In Navier-Stokes equation, continuity equation is employed to describe mass conservation.

$$\nabla \cdot (\rho \mathbf{u}) = 0 \quad \text{Equation 3.36}$$

$$\rho = \frac{PM}{RT} \quad \text{Equation 3.37}$$

$$M = \sum_k x_k M_k \quad \text{Equation 3.38}$$

$\rho$  is the density

$\mathbf{u}$  is the velocity

$M$  is the averaged molar mass

$x_k$  is the molar fraction of species  $k$

$M_k$  is the molar mass of species  $k$

In Brinkman equation, mass conservation is described differently.

$$\nabla \cdot (\rho \mathbf{u}) = Q_{mass} \quad \text{Equation 3.39}$$

$$Q_{mass} = \sum_i R_i \quad \text{Equation 3.40}$$

$Q_{mass}$  is the sum of chemical mass source terms

$R_i$  is the chemical mass source term of species  $i$

$R_i$  is linked to electrode current density via coupling with electrochemistry interface in later section

### 3.3.3.2 Momentum conservation

Flow velocity is solved for via momentum conservation equation. Rather than particle's trajectory of position, the solution implies a field which is defined at each point within certain confined space during certain interval of time. Beginning with calculated velocity field, other quantities of interest like pressure could be computed with aid of extra coupling equation like mass continuity equation.

Within gas channel, momentum conservation of flow is described by Navier-Stokes equation [29].

$$\rho(\mathbf{u} \cdot \nabla)\mathbf{u} = \nabla \cdot \left[ -P\mathbf{I} + \mu(\nabla\mathbf{u} + (\nabla\mathbf{u})^T) - \frac{2}{3}\mu(\nabla \cdot \mathbf{u})\mathbf{I} \right] \quad \text{Equation 3.41}$$

$\rho(\mathbf{u} \cdot \nabla)\mathbf{u}$  is the inertial force term

$-\nabla \cdot (P\mathbf{I})$  is the pressure force term

$\mathbf{I}$  is the identity matrix

$\nabla \cdot (\mu(\nabla\mathbf{u} + (\nabla\mathbf{u})^T) - \frac{2}{3}\mu(\nabla \cdot \mathbf{u})\mathbf{I})$  is the viscous force term

$\mu$  is the dynamic viscosity

Within porous electrode, momentum conservation of flow is described by Brinkman equation. Brinkman equation is well suited for transitions between the flow in porous electrode and the flow in gas channel [29].

$$\left( \frac{\mu}{\kappa} + Q_{mass} \right) \mathbf{u} = \nabla \cdot \left[ -P\mathbf{I} + \frac{\mu}{\varepsilon}(\nabla\mathbf{u} + (\nabla\mathbf{u})^T) - \frac{2}{3}\frac{\mu}{\varepsilon}(\nabla \cdot \mathbf{u})\mathbf{I} \right] \quad \text{Equation 3.42}$$

$-\nabla \cdot (P\mathbf{I})$  is the pressure force term

$\nabla \cdot \left( \frac{\mu}{\varepsilon} (\nabla \mathbf{u} + (\nabla \mathbf{u})^T) - \frac{2\mu}{3\varepsilon} (\nabla \cdot \mathbf{u}) \mathbf{I} \right)$  is the viscous force term

$\kappa$  is the permeability of electrode

$\varepsilon$  is the porosity of electrode

Species	Viscosity ( $\times 10^{-5} Pa \cdot s$ )
$H_2$	$-4 \times 10^{-7} T^2 + 0.0021T + 0.3070$
$H_2O$	$7 \times 10^{-7} T^2 + 0.0032T + 0.0336$
$N_2$	$-2 \times 10^{-6} T^2 + 0.0053T + 0.3355$
$O_2$	$-2 \times 10^{-6} T^2 + 0.0063T + 0.3608$

Table 3.4 The viscosities of the relevant gaseous species

### 3.3.3.3 Initial values

The initial condition of the pressure and velocity fields on both anode and cathode sides are preset as zero.

### 3.3.3.4 Boundary condition

The inlet condition is characterized by inlet mass flow rates of air and fuel, which can be defined by volumetric flow rates, species densities and species molar fractions.

$$m_{an} = (\rho_{H_2}^0 x_{H_2}^0 + \rho_{H_2O}^0 x_{H_2O}^0) Q_{an} \quad \text{Equation 3.43}$$

$$m_{ca} = (\rho_{O_2}^0 x_{O_2}^0 + \rho_{N_2}^0 x_{N_2}^0) Q_{ca} \quad \text{Equation 3.44}$$

$m_{an}$  is the mass flow rate at fuel channel inlet

$m_{ca}$  is the mass flow rate at air channel inlet

$Q_{an}$  is the volumetric flow rate at fuel channel inlet

$Q_{ca}$  is the volumetric flow rate at air channel inlet

$x_i^0$  is molar fraction of species  $i$  at channel inlet

$\rho_i^0$  is density of species  $i$  at channel inlet

The outlet flows are assumed to exhibit operating pressure.

The side surfaces which exclude flow inlet/outlet and symmetric axis are characterized by No slip condition, implying stationary fluid on it.

### 3.3.3.5 Coupling

A mass source based on electrode current density in an electrochemistry interface is defined.

$$R_i = \frac{\nu_i i_v}{nF} M_i \quad \text{Equation 3.45}$$

$R_i$  is the chemical mass source of species  $i$

$\nu_i$  is the stoichiometric coefficient of species  $i$

$i_v$  is the volume-specific current density

$n$  is the number of electrons

$M_i$  is the molar mass of species  $i$

## 3.4 Methodology and Software

### 3.4.1 Discretization

Comsol employs discretization to split the entire domain of interest into discrete sub-domains for solving the equations describing charge, mass/species, and momentum balances. The description of physical laws for space or time dependent problems are usually expressed in terms of partial differential equations. For the most of geometries and problems, those partial differential equations can not be solved analytically. Instead of that, an approximation of the equations can be established, which is based on discretization. A discretization method approximate partial differential equation with numerical model equation, which can be solved numerically. The solution to numerical model equation, in turn, is an approximation to of real solution to partial differential equation. The finite element method is used as discretization manner, which will be elaborated in Appendix.

### 3.4.2 Mesh

The meshing of the full geometry is shown in 3 separate components in Figure 3.3. The established mesh involves 20932 domain elements in it. The entire geometry is discretized by two kinds of meshing: mapped and triangular, accounting for 3680 and 17252 elements respectively. Mapped mesh, as a sort of structured mesh, is applied on the cell of regular geometry, which consists of the anode, the electrolyte, and the cathode. Triangular mesh, as a sort of unstructured mesh, is applied on U-shaped air and fuel channels. Meshing in the vicinity of sensitive regions such as the corners of channels and intersections of SOFC are refined to get more accurate simulation result.

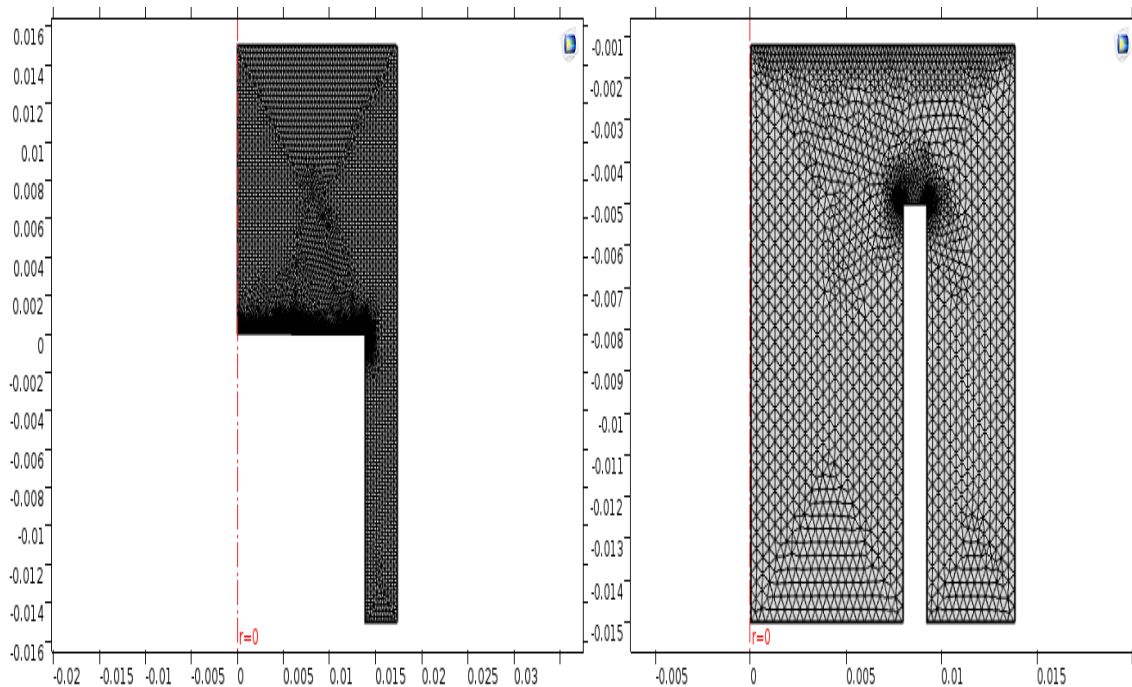


Figure 3.3 (a) Mesh of cathode channel

Figure 3.3 (b) Mesh of anode channel

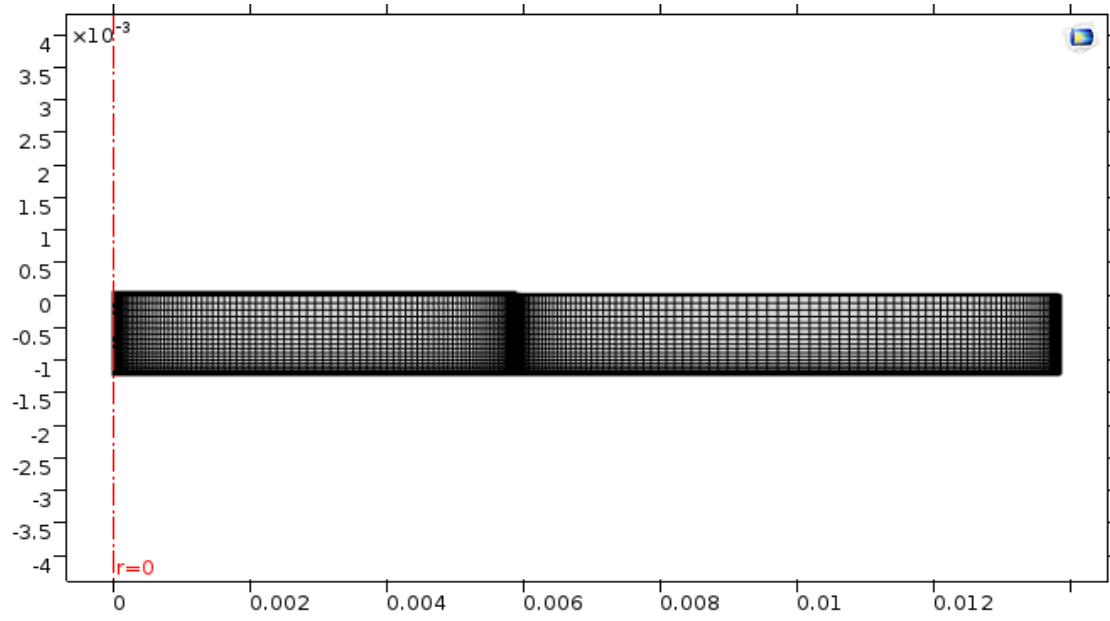


Figure 3.3 (c) Mesh of SOFC

### 3.4.3 Convergence

Convergence is a key factor indicating the reliability of data. In the Comsol model, a fully coupled approach is introduced for solving the steady-state Multiphysics problem. The approach considers all the physics involved in the model at the same time and solves the couplings between the physics simultaneously. The fully coupled solver starts from an initial guess and applies Newton-Raphson iterations until the solution has converged as illustrated below.

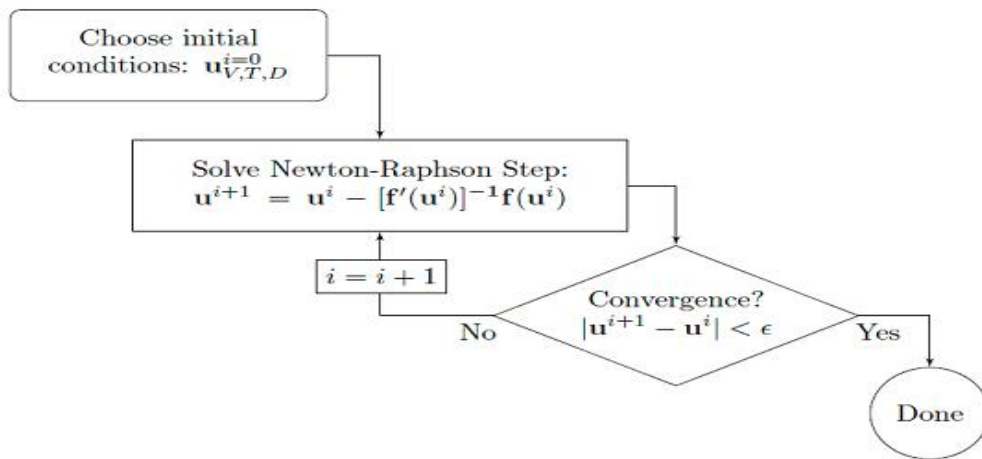


Figure 3.4 The schematics of fully coupled approach

The model is verified for the conservation of mass and charge when relative tolerance factor is lower than  $10^{-12}$ .

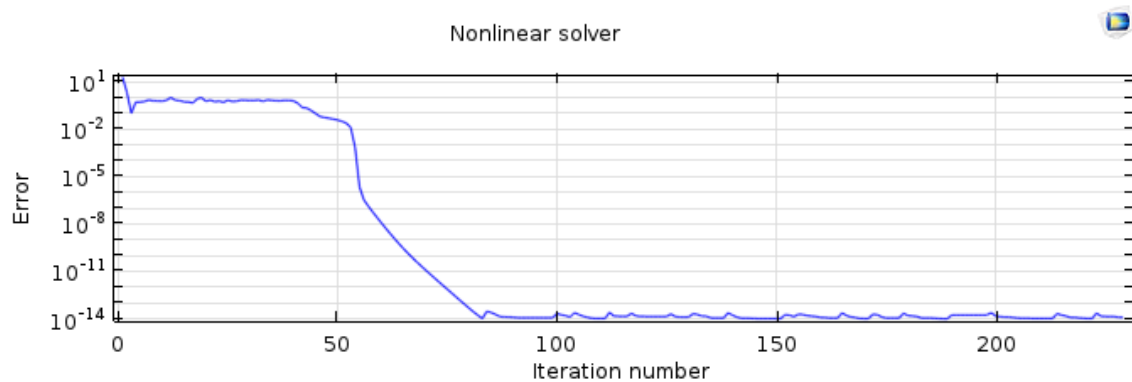


Figure 3.5 The convergence plot of relative error

Theoretically speaking, the consumed fuel should correspond to the cell current as below:

$$\frac{\dot{m}_{an\_in} - \dot{m}_{an\_out}}{M_{H_2}} = \frac{I_{cell}}{nF} \quad \text{Equation 3.46}$$

$\dot{m}_{an\_in}$  is the fuel influx

$\dot{m}_{an\_out}$  is the fuel outflux

$M_{H_2}$  is the molar weight of  $H_2$

$I_{cell}$  is the cell current

$n$  is the number of participating electrons

$F$  is the Faraday constant

During the study,  $\dot{m}_{an,in}$ ,  $\dot{m}_{an,out}$  and  $I_{cell}$  are unknowns to compute. After some iterations, those unknowns converged to constant values as shown in Fig 3.6.

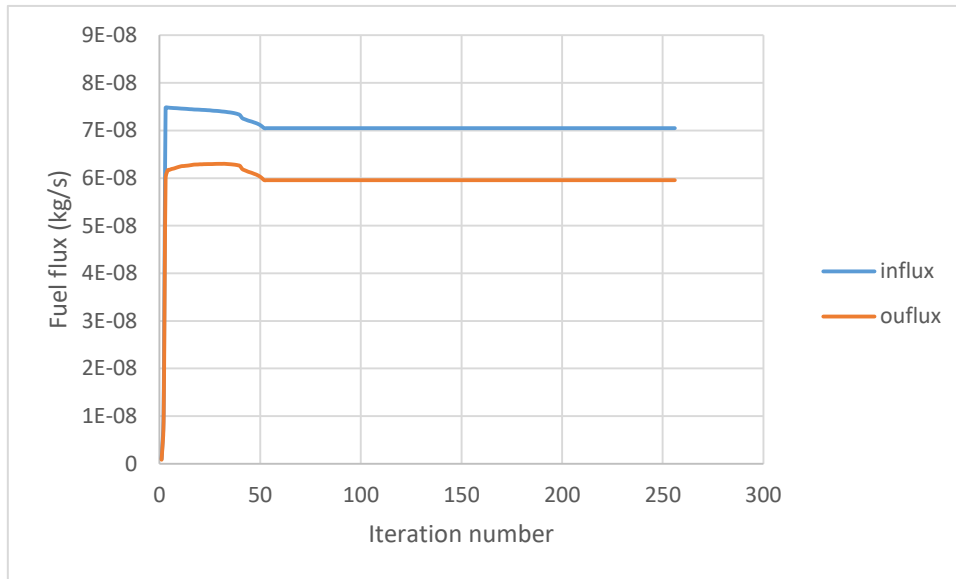


Figure 3.6 (a) The convergence plot of fuel flux

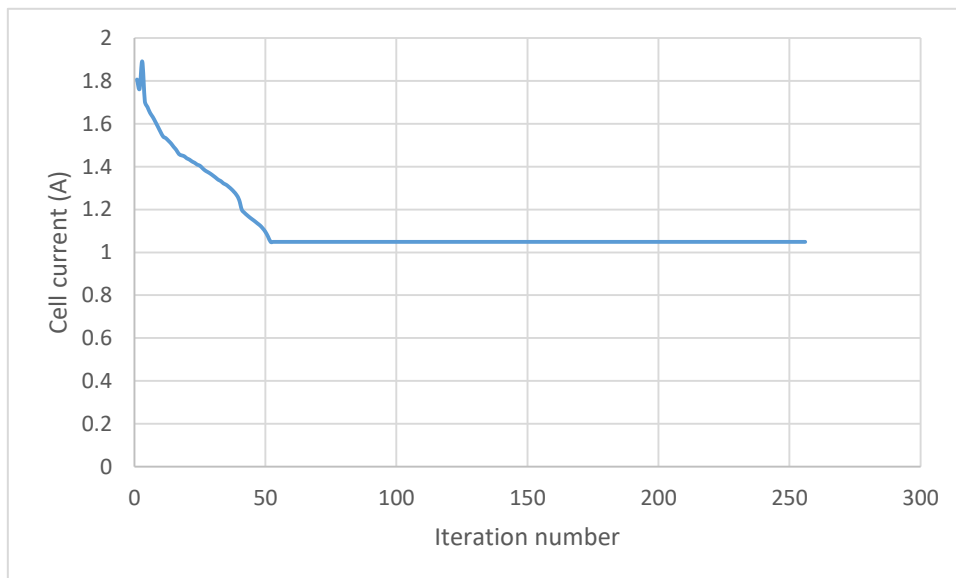


Figure 3.6 (b) The convergence plot of cell current

What's more, the left hand side of Equation 3.46 can be calculated based on fuel influx and fuel outflux. The right hand side of Equation can be calculated based on the cell current. The results on both sides imply the molar consumption rate of fuel. Their relative difference is plotted as a function of iteration number.

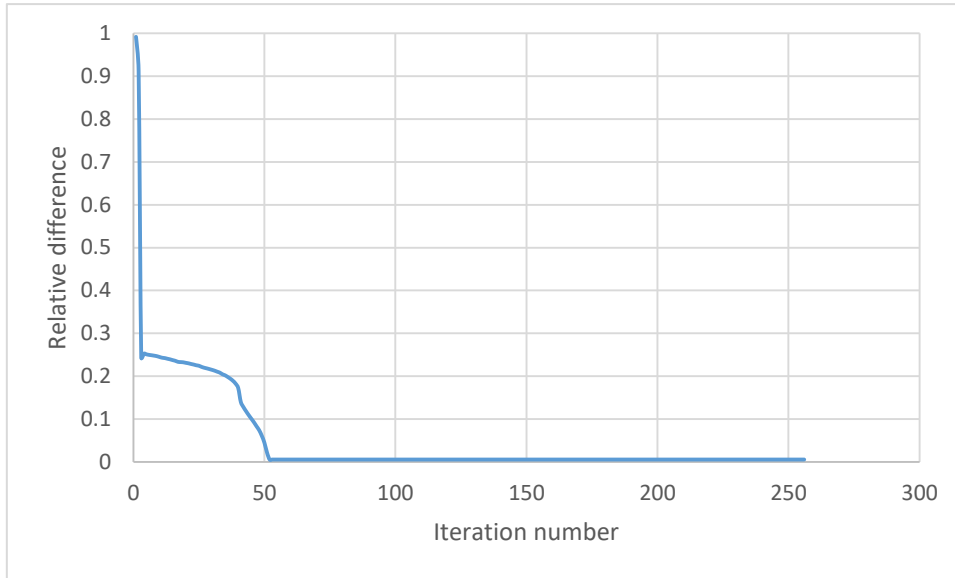


Figure 3.6 (c) The convergence plot of relative difference

As can be seen from Fig, the relative difference between the left hand side and the right hand side is approaching zero once the iteration number reaches 50. After that, it can be assumed that the mass and charge conservations are converged.

# 4

## Results and Discussion

Based on pre-derived TPB-based kinetics, polarization curve indicating current-voltage relationship is simulated under a given cell voltage range and a given fuel composition. The simulated curves are then fitted to the experimental ones for validation. The model is then used to understand overpotential breakdown, species distribution and current distribution. In addition, a parametric study is conducted to analyze the influence of geometric and operating variables on the cell performance.

Geometrical parameters, material properties and operating conditions are tabulated respectively.

Geometrical parameters	Value	Units
Anode radius [25]	0.01385	<i>m</i>
Anode thickness [19]	1220	$\mu m$
Electrolyte radius [35]	0.01385	<i>m</i>
Electrolyte thickness [25]	10	$\mu m$
Cathode radius [25]	0.59173	<i>cm</i>
Cathode thickness [19]	30	$\mu m$

Table 4.1 Geometrical parameters of the SOFC

Material properties	Value	Units
Anode porosity [19]	0.35	
Anode tortuosity [19]	3.5	
Anode permeability [30]	$1.0 \times 10^{-12}$	$m^2$
Anode pore radius [19]	0.50	$\mu m$
Anode specific catalyst area [19]	1080	$cm^2/cm^3$
Anode electronic conductivity [30]	$9.7 \times 10^7 \times \frac{1}{T} \times \exp(-\frac{1150}{T})$	<i>S/m</i>
Ionic conductivity [30]	$3.34 \times 10^4 \times \exp(-\frac{10300}{T})$	<i>S/m</i>
Cathode porosity [19]	0.35	
Cathode tortuosity [19]	3.5	
Cathode permeability [30]	$1.0 \times 10^{-12}$	$m^2$
Cathode pore radius [19]	0.50	$\mu m$
Cathode specific catalyst area	1080	$cm^2/cm^3$

[19]		
Cathode electronic conductivity [30]	$4.2 \times 10^7 \times \frac{1}{T} \times \exp\left(-\frac{1200}{T}\right)$	<i>S/m</i>

Table 4.2 Material properties of the SOFC

Operating conditions	Value	Units
Fuel flow rate [25]	140	<i>ml/min</i>
Air flow rate [25]	550	<i>ml/min</i>
Molar fraction of inlet hydrogen	0.85/0.50/0.20	
Open circuit voltage	0.975/0.887/0.844	<i>V</i>
Operating temperature [25]	800	<i>°C</i>
Operating pressure [25]	1	<i>atm</i>

Table 4.3 Operating conditions of the SOFC

## 4.1 Polarization curve

3 compositions of humidified hydrogen are studied in this simulation as shown in Figure 4.1. For validation, the experimental data from Jiang and Virkar [25] are used. For convenience, experimental OCVs are used as model inputs rather than calculated ones from the Nernst equation.

As discussed previously, the area-specific exchange current density in the anode is expressed as below

$$i_{a,a}^0 = 2Fk_{r,a_4}(K_4K_3)^{\frac{\beta_{c,a_4}}{2}} \left(\frac{K_6}{K_5}\right)^{1-\frac{\beta_{c,a_4}}{2}} \frac{(K_2 \frac{p_{H_2}}{p_0})^{\frac{\beta_{c,a_4}}{2}} \left(\frac{p_{H_2O}}{p_0}\right)^{1-\frac{\beta_{c,a_4}}{2}}}{1+(K_2 \frac{p_{H_2}}{p_0})^{\frac{1}{2}}} (\varphi l_{v,TPB})/a_v \quad \text{Equation 4.1}$$

$i_{a,a}^0$  is the area-specific exchange current in the anode

$k_{r,a_4}$  is the rate constant of the reverse reaction of Reaction 4

$K_i$  is the equilibrium constant of Reaction  $i$

$\beta_{c,a_4}$  is the cathodic symmetric factor of Reaction 4

$p_k$  is the partial pressure of species  $k$

$l_{v,TPB}$  is the physical volume-specific TPB length in the anode

The typical physical volume-specific TPB length of Ni-YSZ cermet anode is reported to be  $10^{12}$  to  $10^{13} \text{ m} \cdot \text{m}^{-3}$  in James' paper [21]. Accordingly it can be reasonably assumed that  $l_{v,TPB} = 5 \times 10^{12} \text{ m} \cdot \text{m}^{-3}$ .

$\varphi$  is the active portion of volume-specific TPB length in the anode

$\varphi l_{v,TPB}$  is the effective volume-specific TPB length in the anode which quantifies the TPBs actually participating in the electrochemical reaction

$a_v$  is the active catalyst area per unit volume

Since all the terms except  $\varphi$  are known,  $\varphi$  is treated as a fitting parameter to enable the agreement between simulation and experimental curves. Consequently,  $\varphi$  is figured out to be

$5.34 \times 10^{-6}$ . The value of effective volume-specific TPB length is several orders of magnitude lower than the typical physical volume-specific TPB length, implying that only a small fraction of the physical TPBs actually participate in the electrochemical reaction.

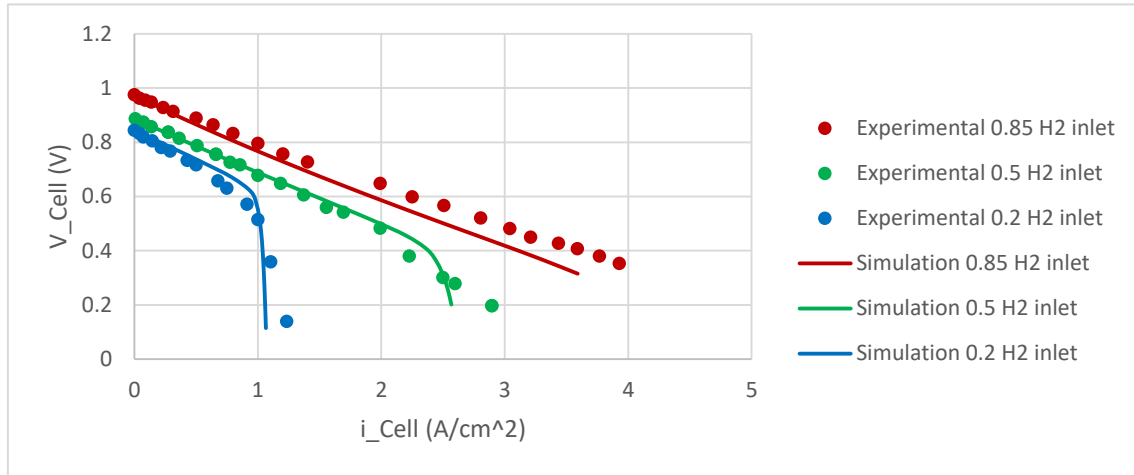


Figure 4.1 Polarization curves at various fuel compositions

The polarization curves in the cases of 85%/50%/20% inlet hydrogen are simulated and validated against Jiang's paper [25]. When inlet hydrogen accounts for 85% molar fraction, within simulation range, cell voltage experiences steady drop as current density increases. When hydrogen composition is 50% or 20%, cell voltage initially decreases in a steady manner and then experiences a rapid drop, with current density limited within a specific level. In the case of 50% inlet hydrogen, voltage rapidly decreases when current density comes to  $2.3 \text{ A/cm}^2$ , confined by limiting current density of  $2.6 \text{ A/cm}^2$ . In the case of 20% inlet hydrogen, voltage rapidly decreases when current density reaches  $0.9 \text{ A/cm}^2$ , restricted by limiting current density of  $1.1 \text{ A/cm}^2$ . The contributions of activation overpotential, Ohmic overpotential and concentration overpotential to entire polarization are investigated in Section 4.3 where the rapid drop of the cell voltage at high current density region in the cases of diluent inlet hydrogen is analyzed and explained as well.

## 4.2 Distribution of gas species

Figure 4.2 shows the molar fractions of gaseous  $H_2$  in fuel channel and in porous anode for the case of 85% inlet  $H_2$  and various cell voltage.

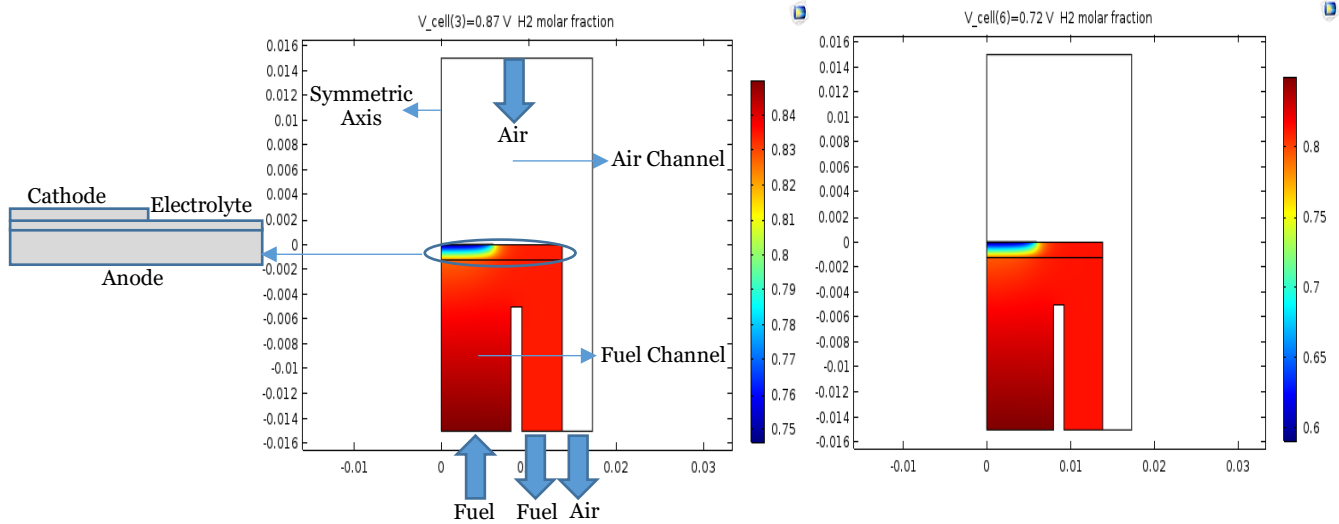


Figure 4.2 (a) Hydrogen distribution at 0.87V

Figure 4.2 (b) Hydrogen distribution at 0.72V

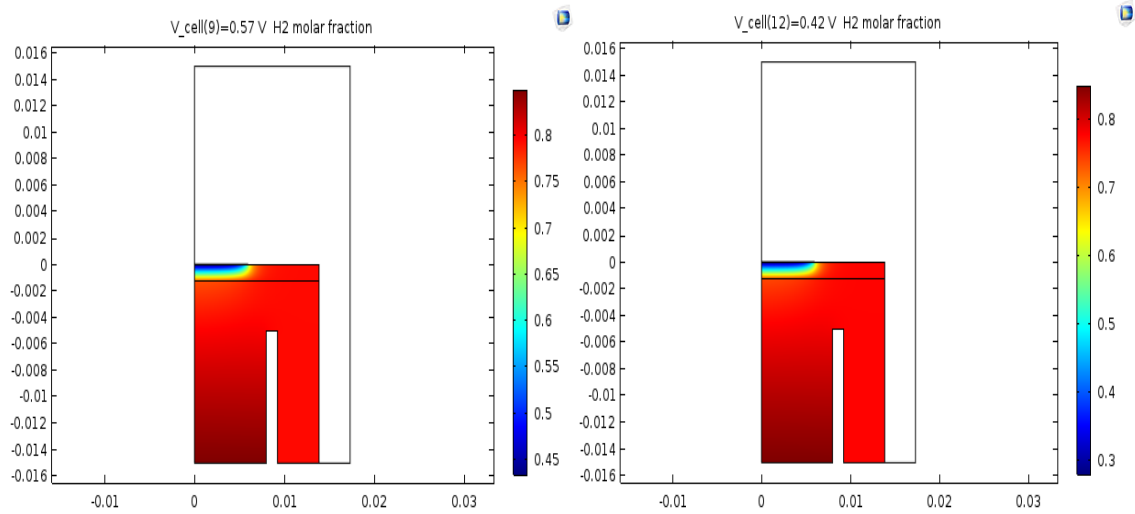


Figure 4.2 (c) Hydrogen distribution at 0.57V

Figure 4.2 (d) Hydrogen distribution at 0.42V

It can be observed that the molar fraction of  $H_2$  first drops slowly in fuel channel and the decrease becomes more rapid when  $H_2$  reaches anode/channel interface toward the anode/electrolyte interface. The gradient of species molar fraction in the anode turns out to be larger than that in the fuel channel, agreeing with the fact that species transport is much slower in the anode because species transport in porous electrode is dominated by diffusion rather than convection [36]. The molar fraction of  $H_2$  leaving the fuel channel allows us to determine the fuel utilization, which is found to be 2.4%/5.9%/9.4%/12.9% at 0.87V/0.72V/0.57V/0.42V. With decreasing cell voltage (or increasing cell current), fuel utilization increases, which is to be

expected.

Figure 4.3 shows the molar fractions of gaseous  $H_2O$  in fuel channel and in porous anode for the case of 85% inlet  $H_2$  and various cell voltage.

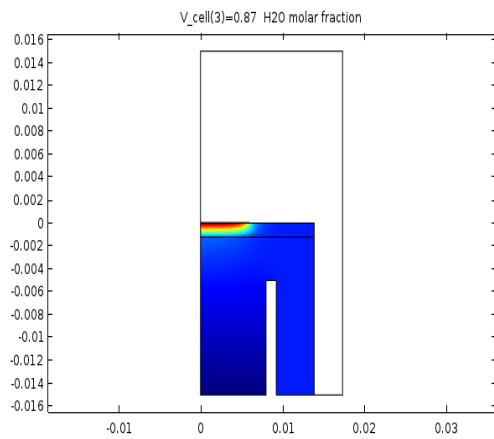


Figure 4.3 (a) Steam distribution at 0.87V

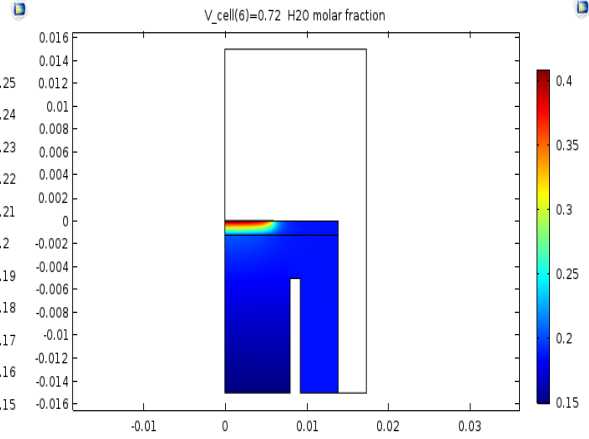


Figure 4.3 (b) Steam distribution at 0.72V

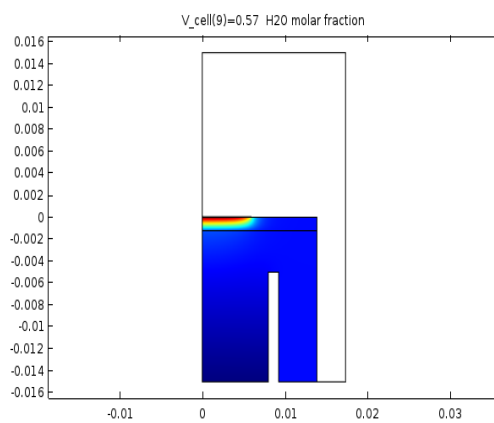


Figure 4.3 (c) Steam distribution at 0.57V

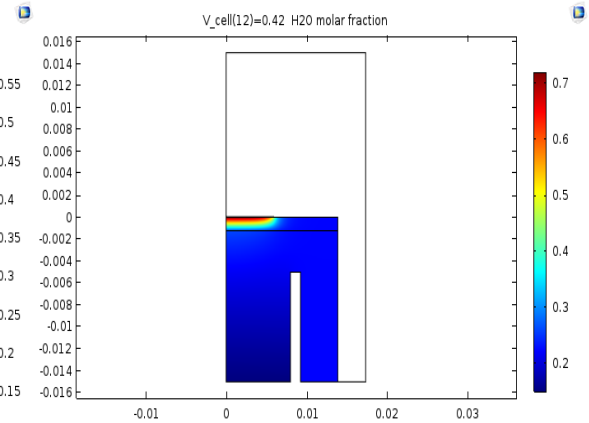


Figure 4.3 (d) Steam distribution at 0.42V

It can also be observed that the molar fraction of  $H_2O$  shows the opposite trend compared to  $H_2$ . It increases more rapidly in the anode region nearby the anode/electrolyte interface where  $H_2$  is converted into  $H_2O$  by  $H_2$  electrochemical oxidation at the active sites in the anode.

Figure 4.4 shows the molar fractions of gaseous  $O_2$  in air channel and in porous cathode for the case of 85% inlet  $H_2$  and various cell voltage.

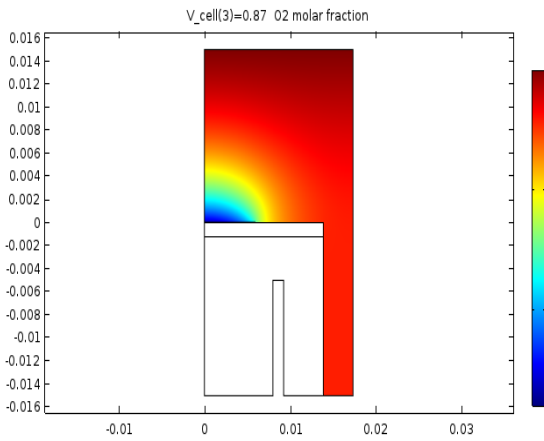


Figure 4.4 (a) Oxygen distribution at 0.87V

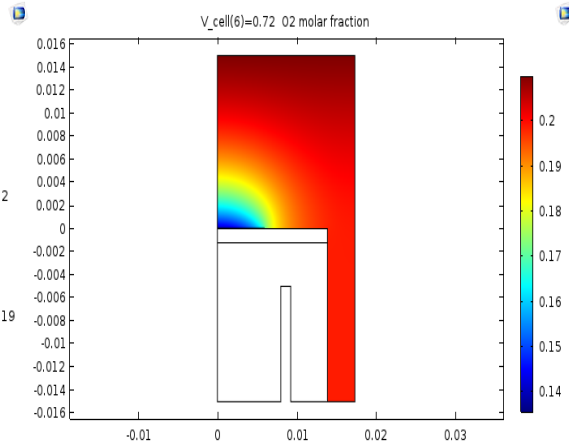


Figure 4.4 (b) Oxygen distribution at 0.72V

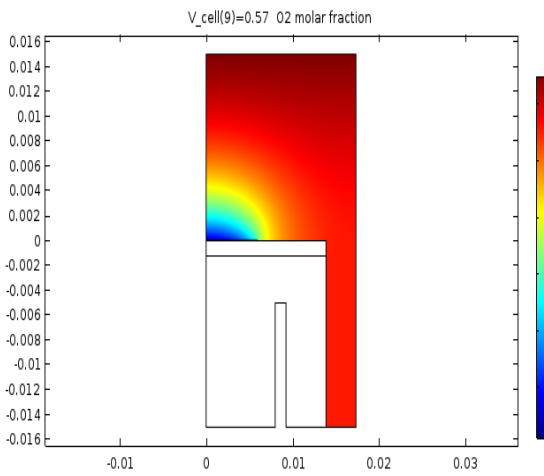


Figure 4.4 (c) Oxygen distribution at 0.57V

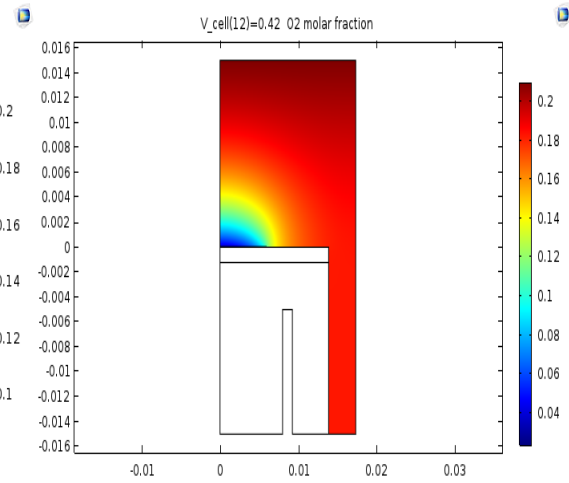


Figure 4.4 (d) Oxygen distribution at 0.42V

Due to tiny thickness of cathode, a slight decrease of  $O_2$  concentration across cathode layer is recognized.

### 4.3 Overpotential breakdown

Once the cell is connected to an electric load, activation overpotential, ohmic overpotential and concentration overpotential would cause a drop in cell voltage.

$$V_{cell} = OCV - \eta_{con,a} - \eta_{con,c} - \eta_{act,a} - |\eta_{act,c}| - \eta_{ohm} \quad \text{Equation 4.2}$$

$V_{cell}$  is the cell voltage

$V_{cell}$  is pre-defined as an input parameter

$OCV$  is open circuit voltage

$OCV$  is pre-determined as an input parameter

$\eta_{act,a}$  is the anode activation overpotential

$\eta_{act,c}$  is the cathode activation overpotential

$\eta_{ohm}$  is the Ohmic overpotential

$\eta_{con,a}$  is the anode concentration overpotential

$\eta_{con,c}$  is the cathode concentration overpotential

The activation overpotential is involved in the Butler-Volmer equation where it is linked to the cell current and species partial pressure.

The area-specific current in the anode is presented by Butler-Volmer form where anode activation overpotential and species partial pressure are involved.

$$i_{a,a} = i_{a,a}^0 \left[ \exp\left(\frac{(\beta_{a,a,4}+1)F\eta_{act,a}}{RT}\right) - \exp\left(-\frac{\beta_{c,a,4}F\eta_{act,a}}{RT}\right) \right] \quad \text{Equation 4.3}$$

$i_{a,a}$  is the area-specific current in the anode

$i_{a,a}^0$  is the area-specific exchange current in the anode

$\beta_{a,a,4}$  is the anodic symmetric factor of Reaction 4 in the anode

$\beta_{c,a,4}$  is the cathodic symmetric factor of Reaction 4 in the cathode

The area-specific current in the anode can be represented by the cell current.

$$i_{a,a} = \frac{I_{cell}}{S_a} \quad \text{Equation 4.4}$$

$I_{cell}$  is the cell current

$S_a$  is the area of the anode

The area-specific exchange current in the anode is a function of the partial pressure of  $H_2$  and the partial pressure of  $H_2O$ .

$$i_{a,a}^0 = 2Fk_{r,a,4}(K_4K_3)^{\frac{\beta_{c,a,4}}{2}} \left(\frac{1}{K_5K_6}\right)^{1-\frac{\beta_{c,a,4}}{2}} \frac{(K_2\frac{p_{H_2}}{p_0})^{\frac{\beta_{c,a,4}}{2}} \left(\frac{p_{H_2O}}{p_0}\right)^{1-\frac{\beta_{c,a,4}}{2}}}{1+(K_2\frac{p_{H_2}}{p_0})^{\frac{1}{2}}} (\phi l_{v,TPB})/a_v \quad \text{Equation 4.1}$$

$k_{r,a,4}$  is the rate constant of the reverse reaction of Reaction 4

$K_i$  is the equilibrium constant of Reaction  $i$

$\beta_{c,a,4}$  is the cathodic symmetric factor of Reaction 4

$p_k$  is the partial pressure of species  $k$

$l_{v,TPB}$  is the physical volume-specific TPB length in the anode

$\phi$  is the active portion of volume-specific TPB length in the anode

$\phi l_{v,TPB}$  is the effective volume-specific TPB length in the anode which quantifies the TPBs actually participating in the electrochemical reaction

$a_v$  is the active specific area

The area-specific current in the cathode is presented by Butler-Volmer form where cathode activation overpotential and species partial pressure are involved.

$$i_{a,c} = i_{a,c}^0 \left[ \exp\left(\frac{\beta_{a,c}F\eta_{act,c}}{RT}\right) - \exp\left(-\frac{\beta_{c,c}F\eta_{act,c}}{RT}\right) \right] \quad \text{Equation 4.5}$$

$i_{a,c}$  is the area-specific current in the cathode

$i_{a,c}^0$  is the area-specific exchange current in the cathode

$\beta_{a,c}$  is the anodic symmetric factor of the cathode reaction

$\beta_{c,c}$  is the cathodic symmetric factor of the cathode reaction

The area-specific current in the cathode can be represented by the cell current.

$$i_{a,c} = \frac{I_{cell}}{S_c} \quad \text{Equation 4.6}$$

$I_{cell}$  is the cell current

$S_c$  is the area of the cathode

The area-specific exchange current in the cathode is a function of the partial pressure of  $O_2$

$$i_{a,c}^0 = i_{O_2}^* \frac{(p_{O_2}/p_{O_2}^*)^{1/4}}{1+(p_{O_2}/p_{O_2}^*)^{1/2}} \quad \text{Equation 4.7}$$

$$p_{O_2}^* = A_{O_2} \exp(-E_{O_2}/RT) \quad \text{Equation 4.8}$$

According to Zhu,  $i_{a,O_2}^* = 2.8 \text{ A/cm}^2$  is obtained [19].

According to Matsuzaki and Yasuda,  $A_{O_2} = 4.9 \times 10^3 \text{ atm}$  and  $E_{O_2} = 200 \text{ kJ}$  are obtained [20].

$p_k$  is the partial pressure of species  $k$

Since the electrolyte's resistance is constant, the Ohmic overpotential is linear to the cell current.

$$\eta_{ohm} = I_{cell} R_{Ohm} \quad \text{Equation 4.9}$$

$$R_{Ohm} = \frac{\sigma_e l_e}{S_e} \quad \text{Equation 4.10}$$

$\eta_{ohm}$  is the Ohmic overpotential

$I_{cell}$  is the cell current

$R_{Ohm}$  is the Ohmic resistance of the cell

$\sigma_e$  is the ionic conductivity of the electrolyte

$l_e$  is the thickness of the electrolyte

$S_e$  is the area of the electrolyte

The concentration overpotential is defined as a function of the partial pressure of species in bulk phase and the partial pressure of species at TPB site, where those pressures are linked to the cell current via coupling terms in the species and mass conservation equations.

$$\eta_{con,a} = \frac{RT}{2F} \ln\left(\frac{p_{H_2}^b}{p_{H_2}^{TPB}} \cdot \frac{p_{H_2O}^{TPB}}{p_{H_2O}^b}\right) \quad \text{Equation 4.11}$$

$$\eta_{con,c} = \frac{RT}{4F} \ln\left(\frac{p_{O_2}^b}{p_{O_2}^{TPB}}\right) \quad \text{Equation 4.12}$$

$p_k^b$  is the partial pressure of species  $k$  in bulk phase

$p_k^{TPB}$  is the partial pressure of species  $k$  at TPB site

For the cell to be studied,  $V_{cell}$  is pre-defined and  $OCV$  is pre-determined. The activation overpotential is involved in the Butler-Volmer equation where it is linked to the cell current and species partial pressures. Since for the case under consideration, the electrolyte's resistance is constant, the Ohmic overpotential is linear to the cell current. The concentration overpotential is defined as a function of the partial pressure of species in bulk phase and the partial pressure of species at TPB site. What's more, species partial pressures are linked to the cell current via coupling terms in the species and mass conservation equations. So all the overpotentials are

functions of the cell current which can be iteratively solved for by Comsol at every stationary state. In every iteration, a value of cell current is assumed, leading to a calculated cell voltage. If the difference between the calculated cell voltage and pre-assigned cell voltage exceeds the preset error tolerance, the iterative study goes on. Otherwise, the iterative study is terminated, with the cell current determined. Furthermore, all the overpotential can be figured out by making use of the cell current.

The anode area-specific exchange current  $i_{a,a}^0$  is a function of molar fraction of hydrogen at TPB site as plotted in Figure 4.5.

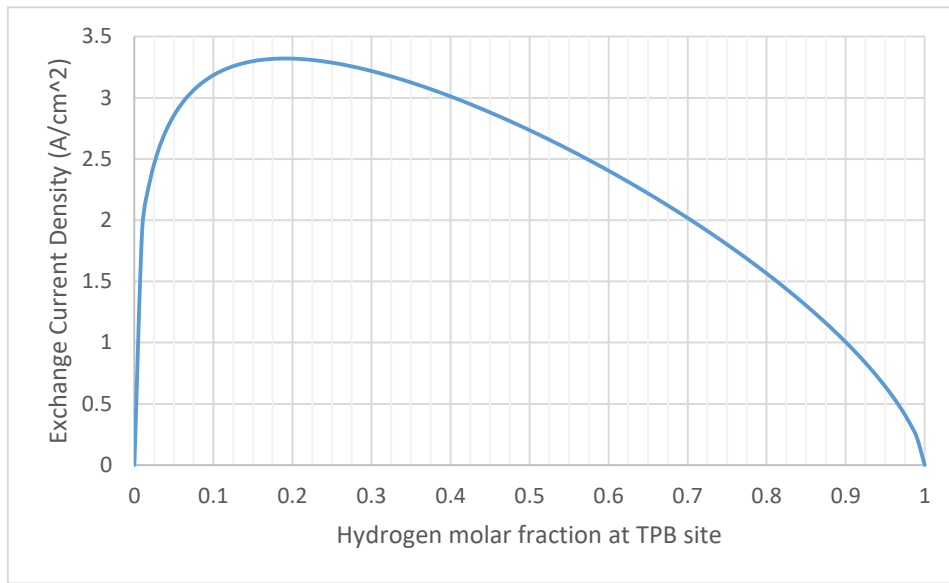


Figure 4.5 Exchange current density as a function of hydrogen molar fraction at TPB site

When the hydrogen molar fraction at TPB site reaches 0.2, the area-specific exchange current achieves its maximum value. When the cell current goes up, the molar fraction falls under 20%, resulting in decreasing area-specific exchange current. Especially, when the cell current keeps rising, the hydrogen molar fraction at TPB site is approaching zero, leading to a rapid drop in the anode area-specific exchange current. In that case, according to the Butler-Volmer equation, the anode activation overpotential will experience a rapid increase consequently.

The contributions of each overpotential when inlet hydrogen occupies 85%, 50%, and 20% molar fractions respectively are shown in Figure 4.5.

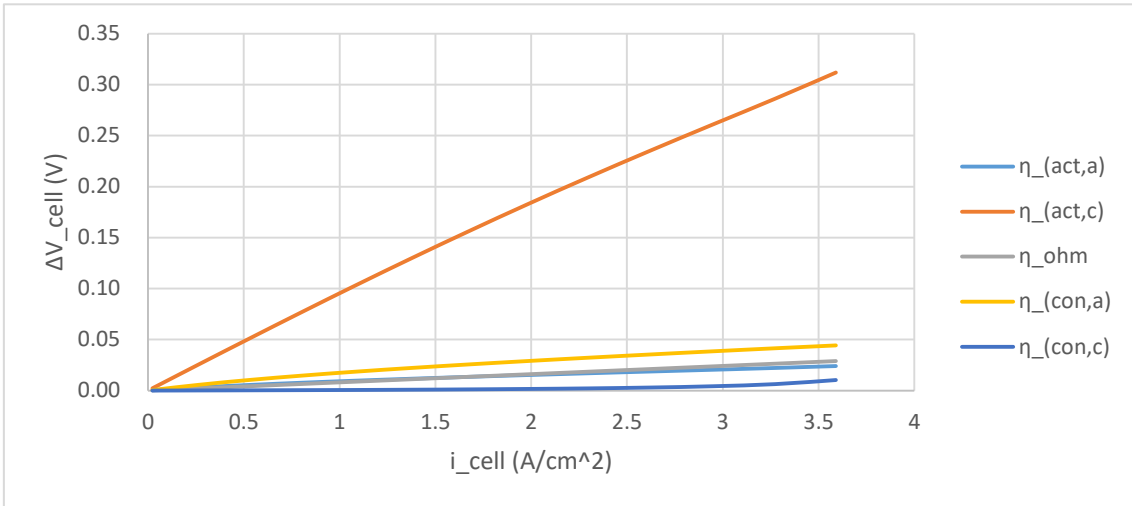


Figure 4.6 (a) Polarization breakdown in the case of 85% hydrogen inlet

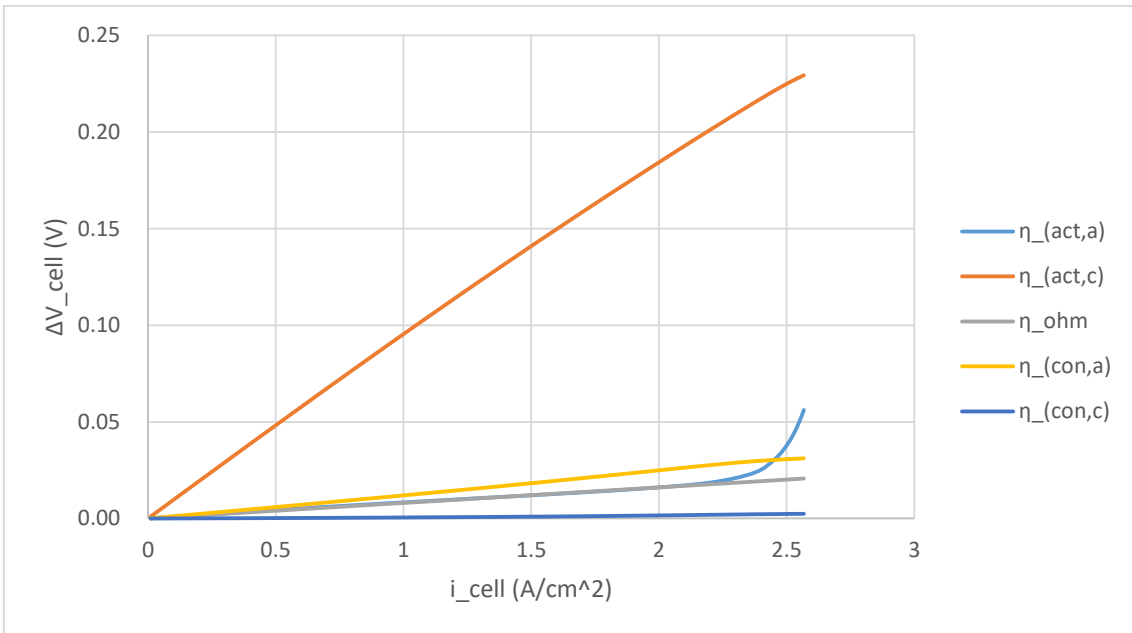


Figure 4.6 (b) Polarization breakdown in the case of 50% hydrogen inlet

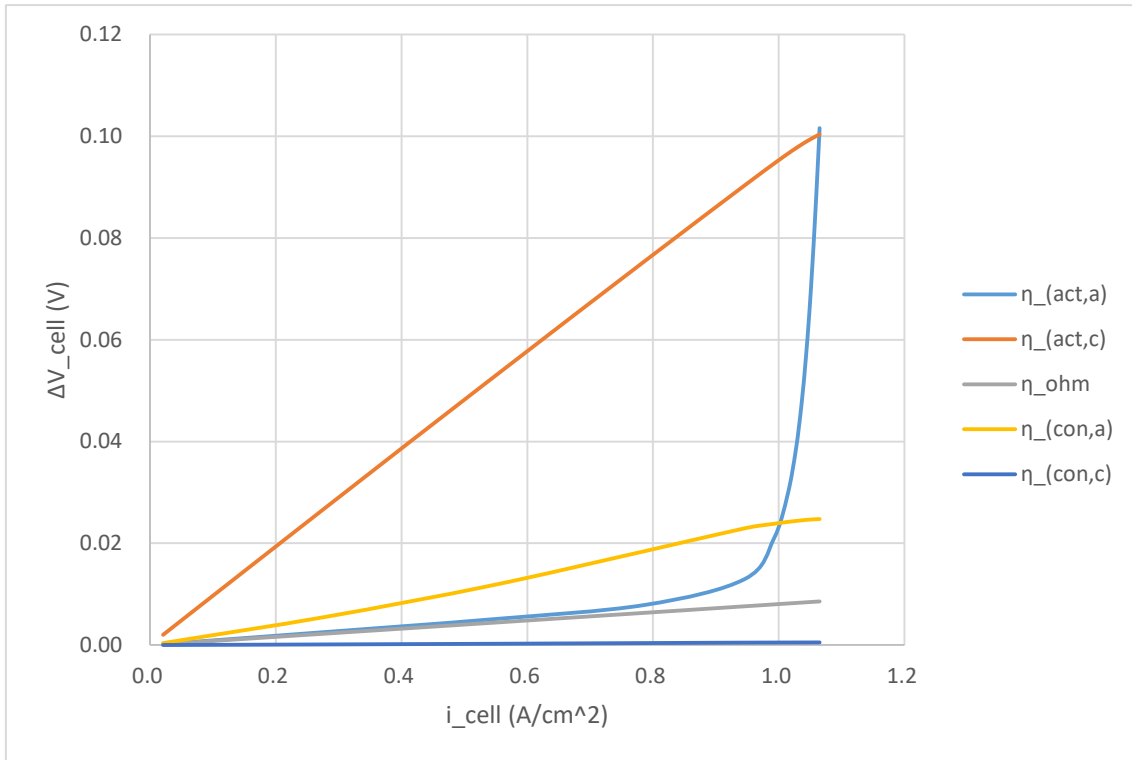


Figure 4.6 (c) Polarization breakdown in the case of 20% hydrogen inlet

Activation overpotential turns to be the most significant loss source. Cathode activation overpotential overwhelms anode activation overpotential. Take the case of 85% hydrogen inlet as an example, when the cell is operated at 0.42V: As has been shown in Figure 4.2 (d), the hydrogen molar fraction within the anode ranges from 0.8 to 0.3, which corresponds to the range of anode area-specific exchange current between  $1.6A/cm^2$  and  $3.2A/cm^2$ ; In contrast, as has been shown in Figure 4.4 (d), the oxygen molar fraction within the cathode is around 0.04, which corresponds to the cathode area-specific exchange current  $1.37A/cm^2$ . The large gap between the anode and cathode area-specific exchange currents could be attributed to the fact that hydrogen oxidation is extremely rapid on a wide range of catalysts like Ni [37]. Such large gap contributes to the large difference in the anode and cathode activation overpotential.

What's more, when the molar fraction of inlet hydrogen is low, say in the case of 20% inlet hydrogen, anode activation overpotential experiences a rapid increase in high current density region, which agrees with the finding observed by Lee [37]. In the case of 20% hydrogen inlet, once cell current density reaches  $0.95 A/cm^2$  which corresponds to 0.6 V cell voltage, anode activation overpotential increases rapidly. The distribution of hydrogen molar fraction along symmetric axis  $r = 0$  at various neighboring cell voltages are presented in Figure 4.7. In addition, the distribution of electrode current density along symmetric axis  $r = 0$  at those cell voltages are presented in Figure 4.8. In Figure 4.7 and Figure 4.8, the horizontal axis denoted by “ $-z$ ” stands for the distance between the point of interest and anode/electrolyte interface. i.e.  $-z = 0$  indicates anode/electrolyte interface;  $-z = 0.00122$  indicates anode/channel interface.

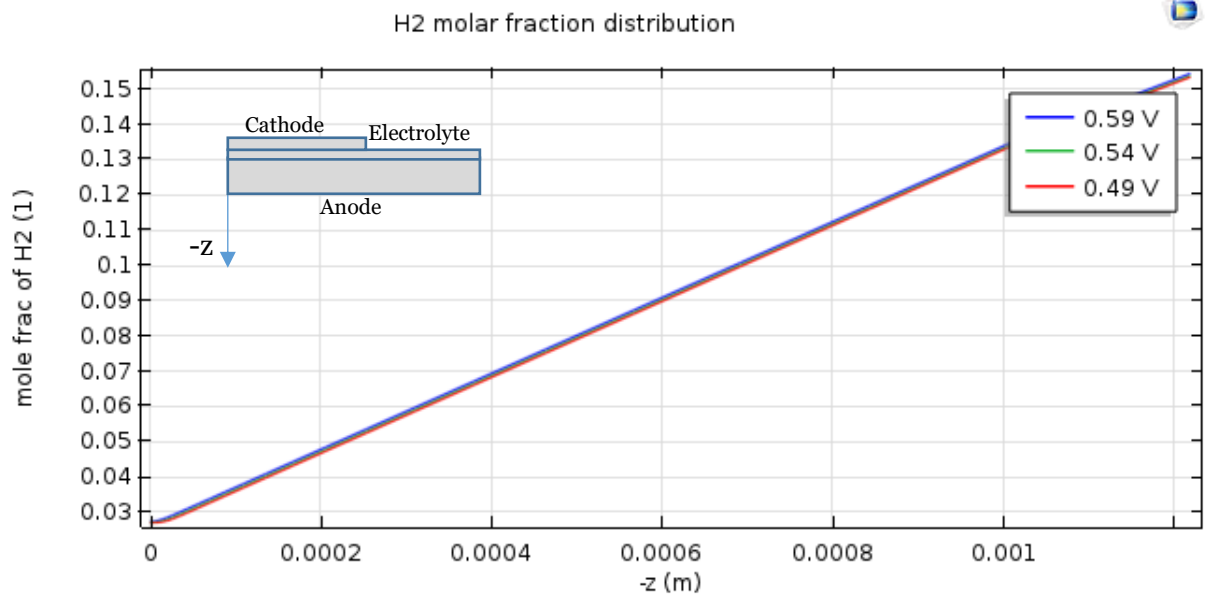


Figure 4.7 (a) Axial distribution of hydrogen molar fraction along entire anode thickness

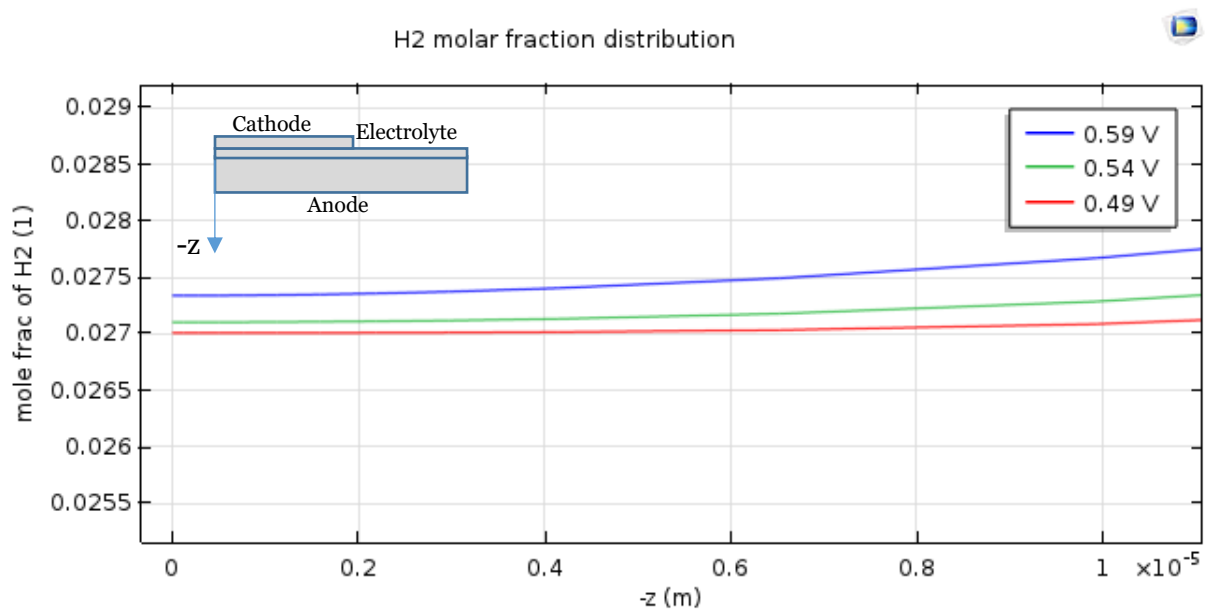


Figure 4.7 (b) Axial distribution of hydrogen molar fraction in the vicinity of anode/electrolyte interface

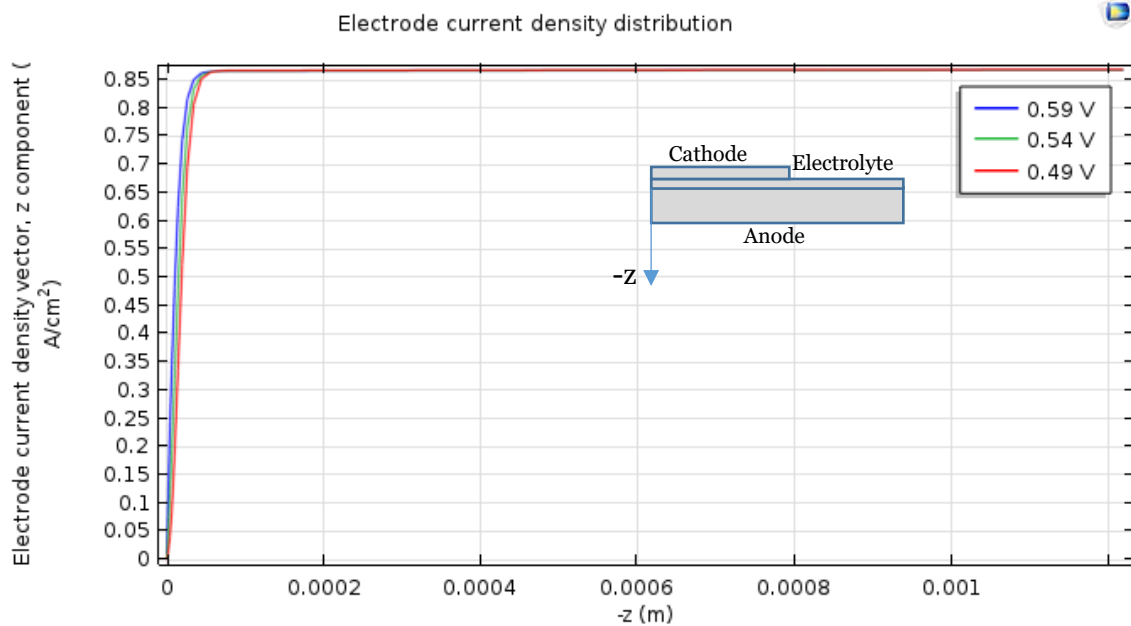


Figure 4.8 Axial distribution of current density along entire anode thickness

When the cell voltage ranges from 0.59V to 0.49V, a rapid increase of current density takes place within a fairly thin layer ( $0 < -z < 0.00005$ ), implying that most of the electrochemical reaction occurs mainly within  $50\mu\text{m}$  distance from the anode/electrolyte interface. Within that distance, hydrogen molar fraction is far less than 20%. With decreasing cell voltage, hydrogen molar fraction approaches zero, causing rapid drop of exchange current density as shown in Fig 4.5. In other words, when current density increases, exchange decreases, implies increased activation overpotential in Butler-Volmer equation. The rapid drop of the exchange current density leads to the rapid increase in anode activation overpotential when cell voltage falls below 0.6V. Furthermore, as can be seen in Figure 4.8, more gradual distribution curve is generated with decreasing cell voltage, leading to a common limiting current density though.

Ohmic overpotential can be clearly recognized as a non-negligible contribution to the overall loss. The Ohmic overpotential is mainly attributed to ionic resistance of electrolyte, which is assumed to be thermally activated vacancy hopping mechanism [37]. Ohmic overpotential increases linearly with increasing current density, with a constant slope observed.

Concentration overpotential accounts for a non-negligible fraction of overall loss. Anode concentration overpotential increases steadily with current density, comparable to anode activation overpotential, except at high current density region in the cases of 50% or 20% inlet hydrogen where activation overpotential increases exponentially. Cathode concentration overpotential is almost negligible compared to any other overpotential, because of fairly small thickness of cathode layer.

#### 4.4 Effect of temperature

Although the model is isothermal, the system of equations is solved at different operating temperatures to study the influence of operating temperature on the cell performance. The cell polarization curves are obtained at 3 temperature conditions of 700°C, 750°C and 800°C.

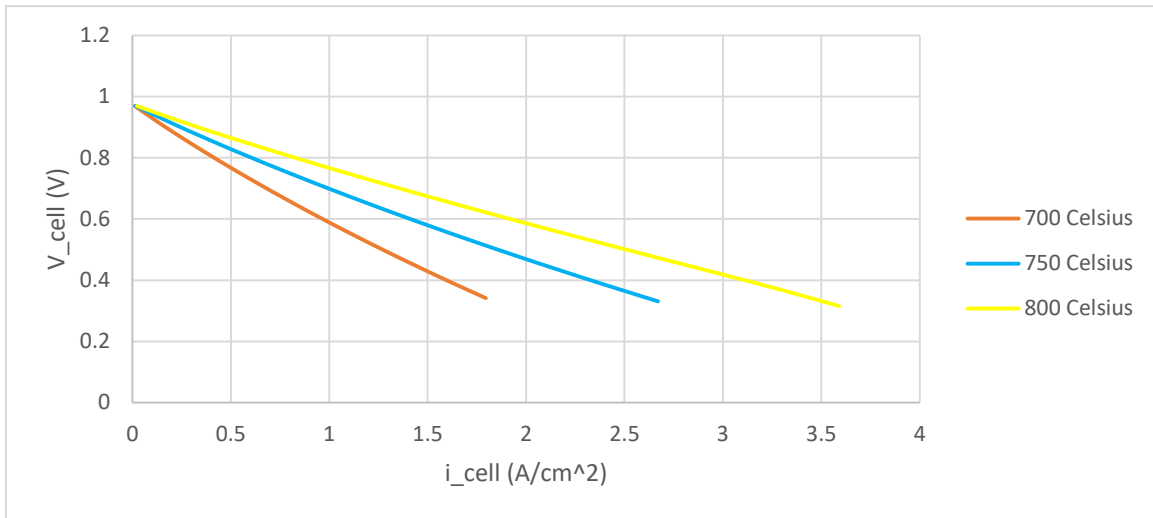


Figure 4.9 Polarization curves at various operating temperatures

It is shown in Figure 4.9 that the cell performance is significantly influenced by the operating temperature. The isothermal assumption might be over simplified. The higher the operating temperature is, the slower drop of cell voltage with respect to cell current is observed. When the cell voltage is fixed, different cell current densities correspond to different operating temperatures. For instance, when the cell voltage is maintained at 0.6V, the cell current densities at 700°C, 750°C and 800°C are 1A/cm<sup>2</sup>, 1.5A/cm<sup>2</sup> and 2A/cm<sup>2</sup> respectively.

As functions of the cell current density, various overpotentials at different operating temperatures are plotted in Figure 4.10.

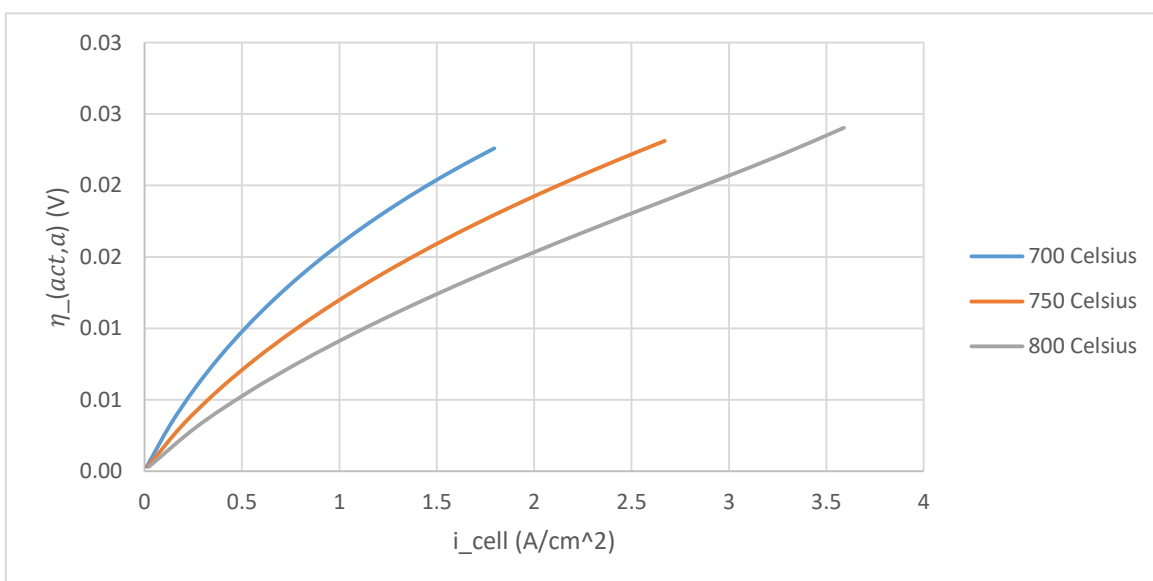


Figure 4.10 (a) Anode activation overpotential at various operating temperatures

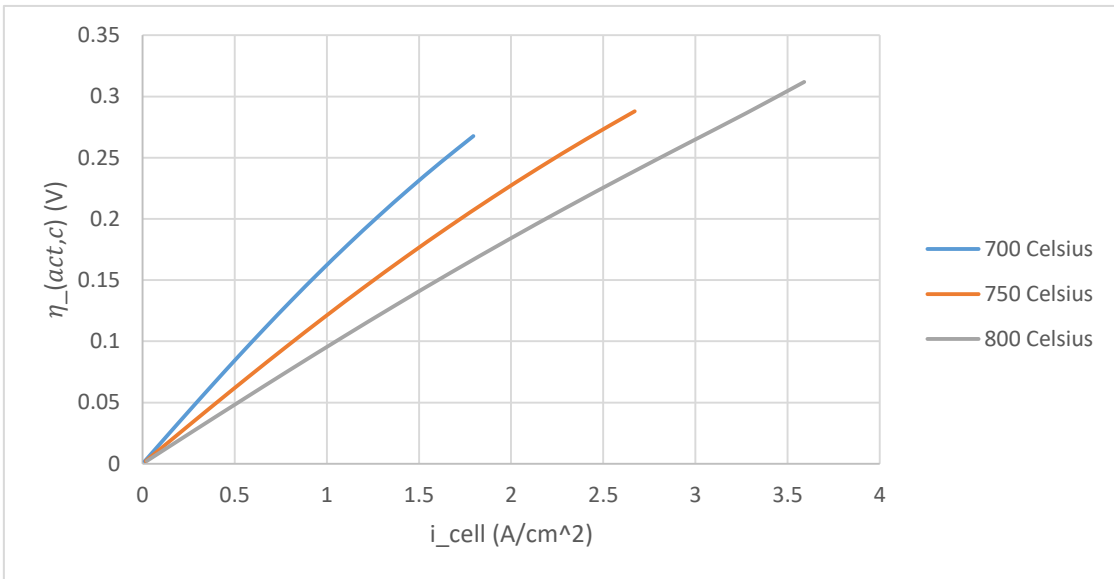


Figure 4.10 (b) Cathode activation overpotential at various operating temperatures

As can be seen in Figure 4.10 (a) and (b) that with increased operating temperature, anode/cathode activation overpotential is reduced at a certain cell current density, which indicates that increased temperature improves the electrode reaction kinetics.

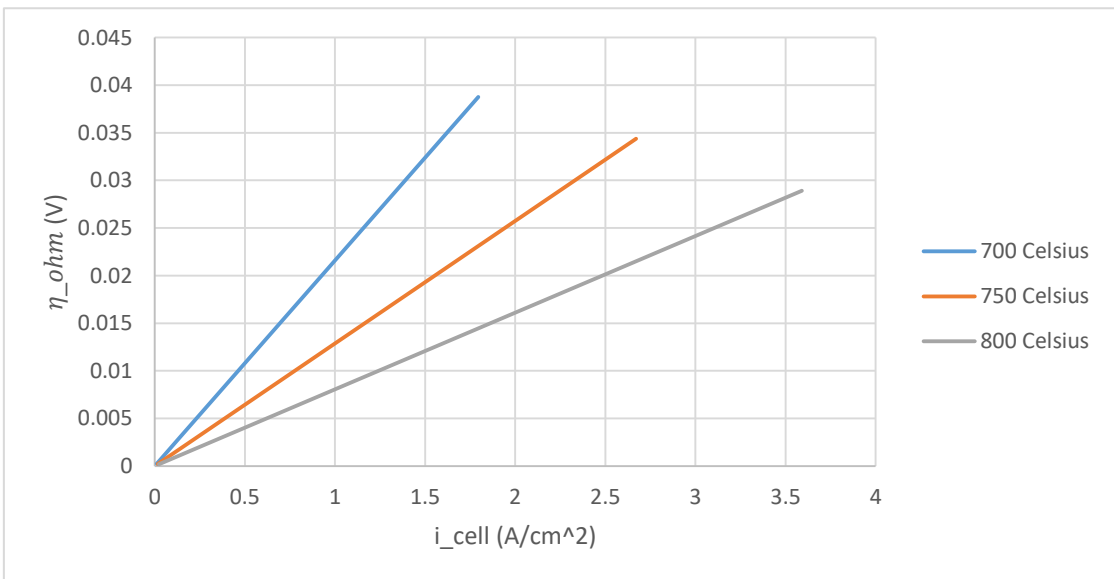


Figure 4.10 (c) Ohmic overpotential at various operating temperatures

As can be seen in Figure 4.10 (c) that with increased operating temperature, Ohmic overpotential is reduced at a certain cell current density, which is due to the fact that increased temperature increases electrolyte conductivity.

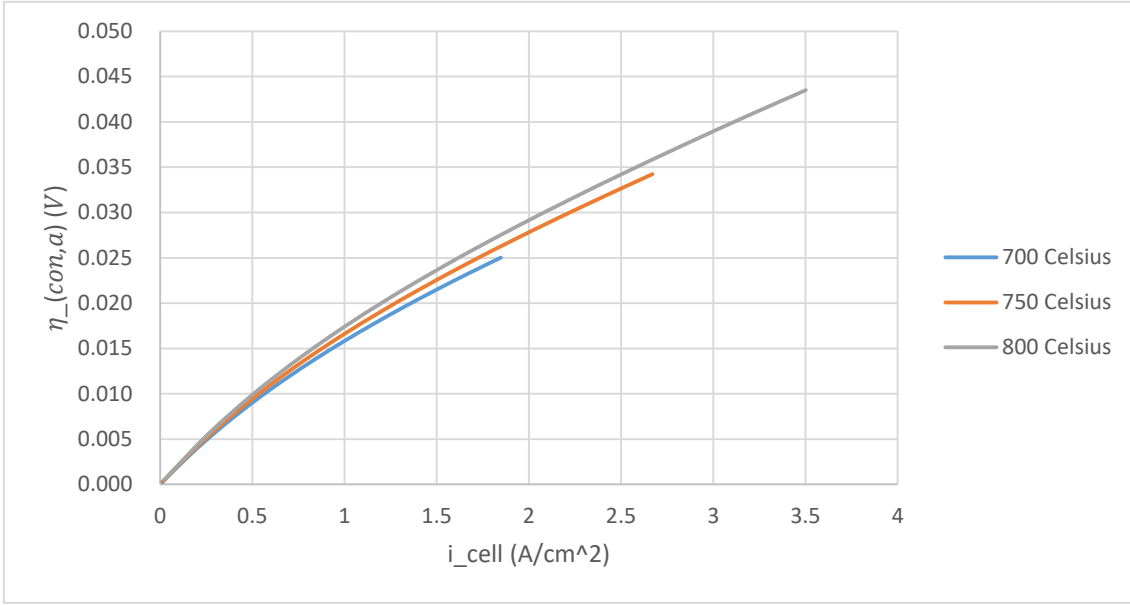


Figure 4.10 (d) Anode concentration overpotential at various operating temperatures

As can be seen in Figure 4.10 (d) that with increased operating temperature, anode concentration overpotential is increased a little bit at a certain cell current density. This result is a bit counterintuitive because mass diffusion generally improves with increasing temperature. So it would be expected that the loss related to mass diffusion would go down. It can be explained using the definition formula of anode concentration overpotential:

$$\eta_{con,a} = \frac{RT}{2F} \ln\left(\frac{p_{H_2}^b}{p_{H_2}^{TPB}} \cdot \frac{p_{H_2O}^{TPB}}{p_{H_2O}^b}\right) \quad \text{Equation 4.11}$$

The first term  $\frac{RT}{2F}$  is linear with respect to the operating temperature  $T$ . It is straightforward that an increased temperature causes increased  $\frac{RT}{2F}$ .

The second term  $\ln\left(\frac{p_{H_2}^b}{p_{H_2}^{TPB}} \cdot \frac{p_{H_2O}^{TPB}}{p_{H_2O}^b}\right)$  is also affected by the operating temperature  $T$ . Considering that increased temperature causes increased binary diffusivity and Knudsen diffusivity, implying higher partial pressure of  $H_2$  at TPB site and lower partial pressure of  $H_2O$  at TPB site, an increased temperature causes decreased  $\ln\left(\frac{p_{H_2}^b}{p_{H_2}^{TPB}} \cdot \frac{p_{H_2O}^{TPB}}{p_{H_2O}^b}\right)$ .

It can be concluded that, the influence of the temperature on the first term  $\frac{RT}{2F}$  exceeds that on the second term  $\ln\left(\frac{p_{H_2}^b}{p_{H_2}^{TPB}} \cdot \frac{p_{H_2O}^{TPB}}{p_{H_2O}^b}\right)$ , leading to the fact that the anode concentration overpotential increases with temperature for a given cell current density.

With increasing operating temperature, electrode activation overpotential and Ohmic overpotential increases significantly while anode concentration overpotential drops a little bit, resulting in the polarization curve where slower drop of cell voltage with respect to cell current

can be observed.

When the cell voltage is maintained at  $0.6V$ , the corresponding cell current density and the corresponding anode concentration overpotential are tabulated at different operating temperatures.

$T$ ( $^{\circ}C$ )	$i_{cell}$ ( $A/cm^2$ )	$\eta_{con,a}$ ( $V$ )
700	1	0.0158
750	1.5	0.0225
800	2	0.0290

Table 4.4 The cell current density and the anode concentration overpotential at  $0.6V$  cell voltage

As has been summarized in Table 4.4, with increasing operating temperature, both the cell current density and the anode concentration overpotential increase. Such behavior is expected to be linked to the species transport processes at different operating temperatures, the distributions of gaseous species along symmetric axis  $r = 0$  at various temperatures at cell voltage  $0.6V$  are plotted in Figure 4.11. The horizontal axis denoted by “ $-z$ ” stands for the distance between the point of interest and anode/electrolyte interface. i.e.  $-z = 0$  indicates anode/electrolyte interface;  $-z = 0.00122$  indicates anode/channel interface.

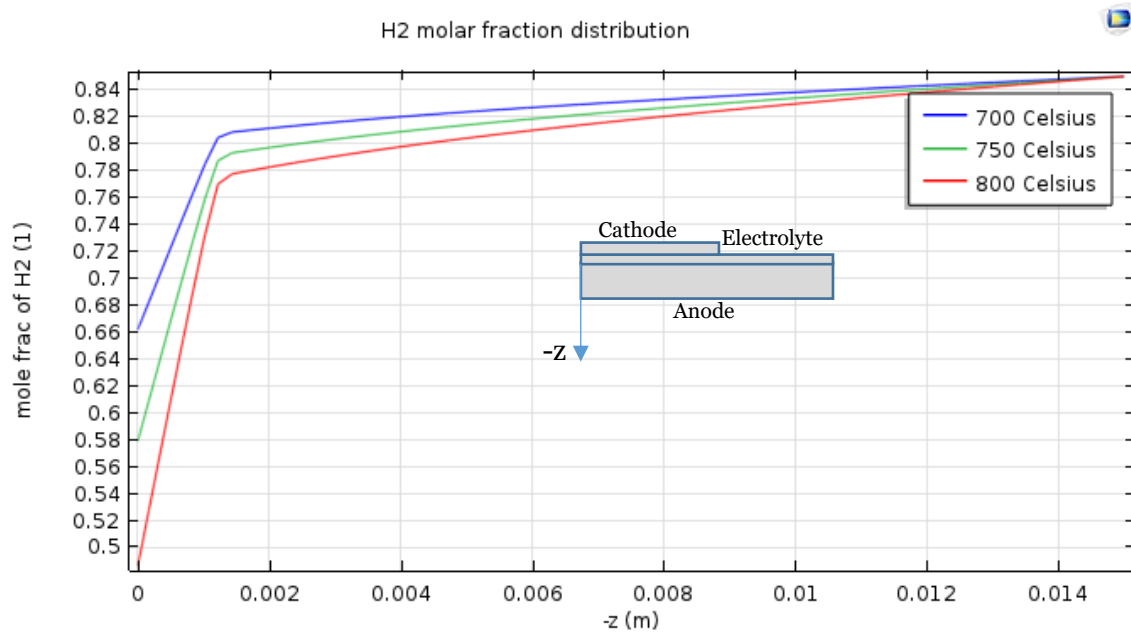


Figure 4.11 (a) Axial distribution of hydrogen molar fraction at various operating temperatures at  $0.6V$

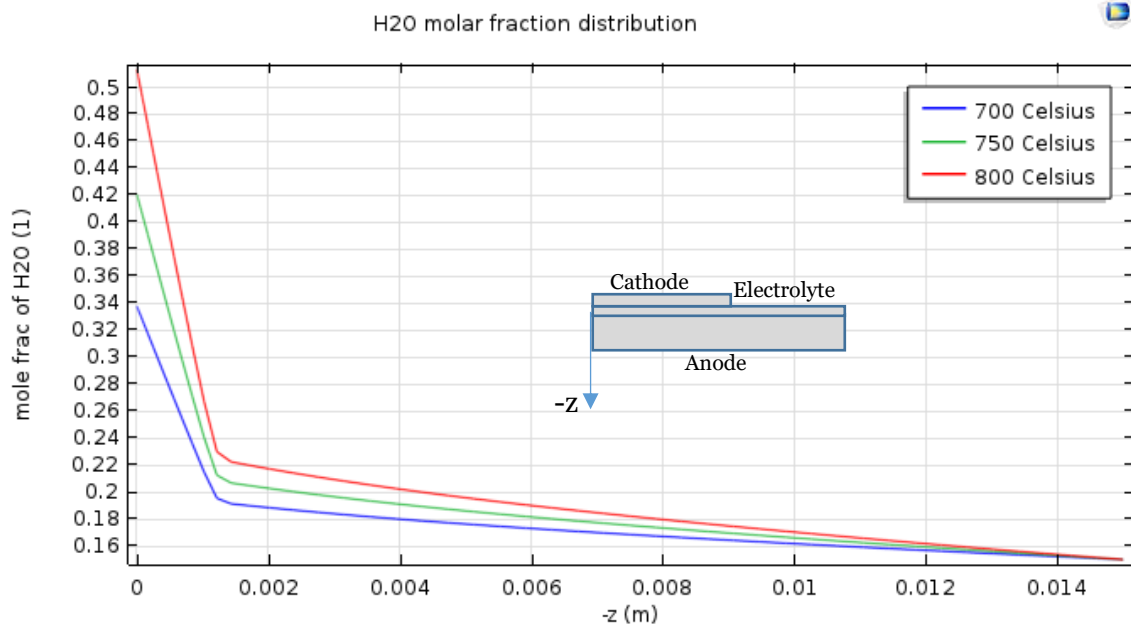


Figure 4.11 (b) Axial distribution of vapor molar fraction at various operating temperatures at 0.6V

Within the fuel channel ( $0.00122 < -z < 0.00122$ ), the molar fraction of hydrogen decreases from channel inlet toward anode/channel interface. Within the anode, the molar fraction of hydrogen decreases from anode/channel interface toward anode/electrolyte interface. The gradient of hydrogen molar fraction within the anode is much larger than that within the fuel channel. Such difference can be attributed to the fact that within the fuel channel, convection dominates the species transport while within the anode, diffusion dominates the species transport where species concentration drops rapidly due to the anode's porous structure.

Within the anode ( $0 < -z < 0.00122$ ), the gradient of hydrogen molar fraction increases with escalating operating temperature, implying that more hydrogen is consumed at higher operating temperature. In contrast, the vapor produced in anode shows opposite trend compared to hydrogen, and the generation of vapor increases with escalating operating temperature. So at a fixed cell voltage, when the operating temperature is raised, fuel consumption and vapor generation within anode are intensified, leading to a larger gradient of species distribution and accordingly a larger concentration overpotential.

# 5

## Conclusions and Outlook

### 5.1 Conclusions

In this project, a TPB based kinetics deriving from pattern Ni anode study is applied to a cermet Ni/YSZ anode. Together with CFD considering molecular, Knudsen and surface diffusions, the TPB based kinetics is incorporated into a mathematical model of humidified hydrogen fed SOFC. Fitting the simulated polarization curves to the lab results helps determining the TPB density in the cermet anode. Based on fitted polarization curves, the established SOFC model is assumed to be valid. The gas species distributions within the SOFC are plotted. Hydrogen and oxygen as reactants show drop in molar fraction as approaching to electrode/electrolyte interface. In contrast, vapor as product shows an opposite trend. With decreasing cell voltage, gaseous species exhibits a larger gradient of molar fraction distribution. On top of that, the overpotential breakdowns in the cases of various inlet fuel compositions are investigated. The cathode activation overpotential contributes the most to the cell's overall voltage loss. According to the derived TPB based kinetics which is built on the detailed insights into the intrinsic processes in the anode, the exchange current density in the anode is presented as a function of hydrogen molar fraction, operating temperature and TPB density. A soaring behavior of the anode activation overpotential at high current density region in the case of diluent inlet hydrogen is recognized, attributed to the depletion of hydrogen in the vicinity of anode/electrolyte interface which is found to be the most electrochemically active region in the anode. Furthermore, the parametric study of operating temperature is conducted to see their effects on SOFC performance. When the operating temperature is lifted, a more gradual polarization curve is generated. At a fixed cell voltage, an increasing operating temperature causes intensified hydrogen consumption and vapor production, leading to increased anode concentration overpotential.

### 5.2 Outlook

In this project, some factors influencing SOFC's performance has been simplified and idealized. TPB sites in reality, are not homogeneously distributed within the anode. With the help of 3D reconstruction of the anode's porous structure, TPB sites' actual distribution can be explored and imaged [21]. Taking such heterogeneity into consideration can definitely approach a more accurate model, with huge computational cost generated though. In addition, the temperature in SOFC is not exactly constant over the entire domain. It has been revealed that the operating

temperature has huge influence on cell performance. With the assistance of energy transport and conservation law, the heat transfer in SOFC can be modelled, allowing the prediction of temperature distribution within the cell [16]. Similarly, such higher fidelity requires extra expense of computation.

# Acknowledgements

One year ago, with the passion for fuel cell, I chose the thesis topic related to SOFC modeling, which was complementary to experimental work conducted in a professional group – Fuel Cell Systems Laboratory. One year later, I was proud and satisfied about my choice and what I have done during this meaningful period. Concurrently, I would like to express my sincere appreciation to the people who has helped me on the thesis and in the life, full of gratitude.

First, I would like to thank my supervisor P.V. Aravind for his valuable advices, supports and long-time discussion to inspire me for deep dig in modeling and help me understand the scientific theory. Besides, I would like to express my gratitude to my daily supervisor AN Tabish for teaching me to apply experimental data and literature results in modeling and improving my academic presentation skills. What's more, I would like to thank Jelle for reviewing my master thesis and giving his comments on that. Additionally, I would like to thank Pradeep for training me how to use Comsol correctly and how to shoot the bugs efficiently.

Furthermore, I would like to thank my roommates and classmates in SET to help me in the life. And Finally, I would like to express my gratitude to my family for their unconditional love and support, from the bottom of my heart.

Last but not least, as the strong voice send from Saudi oil minister three decades ago: “The Stone Age didn't end for lack of stone, and the oil age will end long before the world runs out of oil.”, this would inspire all the engineers from Sustainable Energy Technology Program to strive for a more sustainable future, for us, for everyone.

*JINJUN LI*

*TU Delft library, September 2017*

# Bibliography

- [1] A. B. Stambouli and E. Traversa, "Solid oxide fuel cells (SOFCs): A review of an environmentally clean and efficient source of energy," *Renew. Sustain. Energy Rev.*, vol. 6, no. 5, pp. 433–455, 2002.
- [2] NASA, "Space Applications of Hydrogen and Fuel Cells," p. 2017, 2012.
- [3] U.S. Department of Energy, "Comparison of Fuel Cell Technologies," *Energy Effic. Renew. Energy*, no. February, p. 3463, 2011.
- [4] U.S. Department of Energy, "Fuel Cells," pp. 1–2, 2017.
- [5] F. Wikipedia, "Solid oxide fuel cell," pp. 1–14, 2017.
- [6] S. P. S. Badwal and K. Foger, "Solid oxide electrolyte fuel cell review," *Ceram. Int.*, vol. 22, no. 3, pp. 257–265, 1996.
- [7] D. McLarty, J. Brouwer, and S. Samuelsen, "Fuel cell-gas turbine hybrid system design part I: Steady state performance," *J. Power Sources*, vol. 257, pp. 412–420, 2014.
- [8] B. Shri Prakash, S. Senthil Kumar, and S. T. Aruna, "Properties and development of Ni/YSZ as an anode material in solid oxide fuel cell: A review," *Renew. Sustain. Energy Rev.*, vol. 36, pp. 149–179, 2014.
- [9] J. Li, Z. Bai, and E. Croiset, "A two-dimensional modeling of solid oxide fuel cell button cells with detailed electrochemistry mechanism," *J. Power Sources*, vol. 333, pp. 164–172, 2016.
- [10] K. P. Recknagle, R. E. Williford, L. A. Chick, D. R. Rector, and M. A. Khaleel, "Three-dimensional thermo-fluid electrochemical modeling of planar SOFC stacks," *J. Power Sources*, vol. 113, no. 1, pp. 109–114, 2003.
- [11] H. Yakabe, T. Ogiwara, M. Hishinuma, and I. Yasuda, "3-D model calculation for planar SOFC," *J. Power Sources*, vol. 102, no. 1–2, pp. 144–154, 2001.
- [12] Y. Shi, N. Cai, and C. Li, "Numerical modeling of an anode-supported SOFC button cell considering anodic surface diffusion," *J. Power Sources*, vol. 164, no. 2, pp. 639–648, 2007.
- [13] P. Chinda, S. Chanchaona, P. Brault, and W. Wechsato, "Mathematical Modeling of a Solid Oxide Fuel Cell with Nearly Spherical-Shaped Electrode Particles," *J. Sustain. Energy Environment*, vol. 1, no. August, pp. 185–196, 2010.
- [14] D. A. Noren and M. A. Hoffman, "Clarifying the Butler-Volmer equation and related approximations for calculating activation losses in solid oxide fuel cell models," *J. Power Sources*, vol. 152, no. 1–2, pp. 175–181, 2005.
- [15] A. V. Virkar, J. Chen, C. W. Tanner, and J. W. Kim, "Role of electrode microstructure on activation and concentration polarizations in solid oxide fuel cells," *Solid State Ionics*, vol. 131, no. 1, pp. 189–198, 2000.
- [16] A. Hauch and M. B. Mogensen, *Advances in Medium and High Temperature Solid Oxide Fuel Cell Technology*, vol. 574. 2017.
- [17] M. Vogler, A. Bieberle-Hütter, L. Gauckler, J. Warnatz, and W. G. Bessler, "Modelling Study of Surface Reactions, Diffusion, and Spillover at a Ni/YSZ Patterned Anode," *J. Electrochem. Soc.*, vol. 156, no. 5, pp. 663–672, 2009.
- [18] A. Bieberle, L. P. Meier, and L. J. Gauckler, "The Electrochemistry of Ni Pattern Anodes Used as Solid Oxide Fuel Cell Model Electrodes," *J. Electrochem. Soc.*, vol. 148, no. 6, pp. A646–A656,

- 2001.
- [19] H. Zhu, R. J. Kee, V. M. Janardhanan, O. Deutschmann, and D. G. Goodwin, "Modeling Elementary Heterogeneous Chemistry and Electrochemistry in Solid-Oxide Fuel Cells," *J. Electrochem. Soc.*, vol. 152, no. 12, p. A2427, 2005.
- [20] Y. Matsuzaki and I. Yasuda, "Relationship between the steady-state polarization of the SOFC air electrode,  $\text{La}_{0.6}\text{Sr}_{0.4}\text{MnO}_{3+\delta}/\text{YSZ}$ , and its complex impedance measured at the equilibrium potential," *Solid State Ionics*, vol. 126, no. 3–4, pp. 307–313, 1999.
- [21] J. R. Wilson *et al.*, "Three-dimensional reconstruction of a solid-oxide fuel-cell anode," *Nat. Mater.*, vol. 5, no. 7, pp. 541–544, 2006.
- [22] M. Brown, S. Primdahl, and M. Mogensen, "Structure / Performance Relations for Ni / Yttria-Stabilized Zirconia Anodes for Solid Oxide Fuel Cells," *J. Electrochem. Soc.*, vol. 147, no. 2, pp. 475–485, 2000.
- [23] H. C. Patel, A. N. Tabish, F. Comelli, and P. V. Aravind, "Oxidation of  $\text{H}_2$ , CO and syngas mixtures on ceria and nickel pattern anodes," *Appl. Energy*, vol. 154, pp. 912–920, 2015.
- [24] "Modeling of solid oxide fuel cell performance with coal gasification Modeling of Solid Oxide Fuel Cell Performance with Coal Gasification by," no. October, 2016.
- [25] Y. Jiang and A. V. Virkar, "Fuel composition and diluent effect on gas transport and performance of anode-supported SOFCs," *J. Electrochem. Soc.*, vol. 150, no. 7, pp. A942–A951, 2003.
- [26] Y. Xie and S. Carolina, "Multi-Physicochemical Modeling of Solid Oxide Fuel Cells and Electrolyzer Cells," pp. 53–54, 2013.
- [27] V. Ramani, "Fuel Cells," *Electrochem. Soc. Interface*, pp. 41–44, 2006.
- [28] C. J. Moyer, N. P. Sullivan, H. Zhu, and R. J. Kee, "Polarization Characteristics and Chemistry in Reversible Tubular Solid-Oxide Cells Operating on Mixtures of  $\text{H}_2$ , CO,  $\text{H}_2\text{O}$ , and  $\text{CO}_2$ ," *J. Electrochem. Soc.*, vol. 158, no. 2, pp. B117–B131, 2011.
- [29] COMSOL, *Chemical Engineering MODULE*.
- [30] C. Bao, Z. Jiang, and X. Zhang, "Mathematical modeling of synthesis gas fueled electrochemistry and transport including  $\text{H}_2/\text{CO}$  co-oxidation and surface diffusion in solid oxide fuel cell," *J. Power Sources*, vol. 294, no. April 2016, pp. 317–332, 2015.
- [31] C. Bao, Z. Jiang, and X. Zhang, "Modeling mass transfer in solid oxide fuel cell anode: I. Comparison between Fickian, Stefan-Maxwell and dusty-gas models," *J. Power Sources*, vol. 310, pp. 32–40, 2016.
- [32] G. Correlation and T. Phenomena, "Example 11.1: Prediction of Binary Gas Diffusivities," vol. 58, no. 5, pp. 4–6, 2017.
- [33] C. Bao, Y. Shi, C. Li, N. Cai, and Q. Su, "Mathematical modeling of solid oxide fuel cells at high fuel utilization based on diffusion equivalent circuit model," *AIChE J.*, vol. 56, no. 5, pp. 1363–1371, 2010.
- [34] B. Carasi, "Compressibility Operations and Buoyancy Forces for Flow Simulations Compressibility Operations for the Navier-Stokes Equations in COMSOL Multiphysics®," 2016.
- [35] Y. Jiang, A. V. Virkar, and F. Zhao, "The Effect of Testing Geometry on the Measurement of Cell Performance in Anode-Supported Solid Oxide Fuel Cells: The Effect of Cathode Area," *J. Electrochem. Soc.*, vol. 148, no. 10, p. A1091, 2001.
- [36] Z. Zhang *et al.*, "Three-dimensional CFD modeling of transport phenomena in a cross-flow anode-supported planar SOFC," *Energies*, vol. 7, no. 1, pp. 80–98, 2014.

- [37] W. Y. Lee, D. Wee, and A. F. Ghoniem, "An improved one-dimensional membrane-electrode assembly model to predict the performance of solid oxide fuel cell including the limiting current density," *J. Power Sources*, vol. 186, no. 2, pp. 417–427, 2009.

